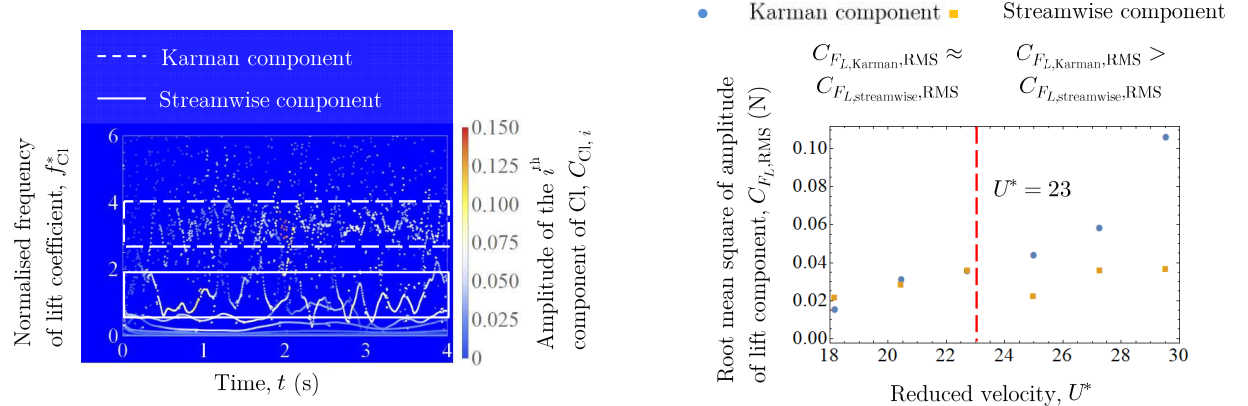


1 Graphical Abstract

2 Temporal Evolution of Lift in a Pure Cruciform System for Energy Harvesting

3 Ahmad Adzlan,Mohamed Sukri Mat Ali



4 Highlights

5 Temporal Evolution of Lift in a Pure Cruciform System for Energy Harvesting

6 Ahmad Adzlan,Mohamed Sukri Mat Ali

- 7** • Decomposition of the lift coefficient signal makes apparent the superposition of the lift generated by the shed-
8 ding of Karman and streamwise vortices, once the streamwise vortex shedding becomes the dominant driving
9 mechanism for vibration.
- 10** • Determination of phase lag between lift and cylinder displacement using Hilbert-Huang Transform reveals the
11 characteristics of an initial branch at the onset of streamwise vortex-induced vibration: evidence supporting the
12 view that the onset of streamwise vortex is sudden rather than gradual.
- 13** • Computation of the ratio of contribution to the total lift amplitude from the shedding of both Karman and stream-
14 wise vortices suggest that we might be able to enlarge the RMS amplitude, and thus harnessed power, if we can
15 redirect energy away from Karman vortices towards streamwise vortices, in a streamwise vortex-dominated vi-
16 bration regime.

¹⁷ Temporal Evolution of Lift in a Pure Cruciform System for Energy ¹⁸ Harvesting

¹⁹ Ahmad Adzlan^{a,b,*}, Mohamed Sukri Mat Ali^a

²⁰ ^aMalaysia-Japan International Institute of Technology, Universiti Teknologi Malaysia, 54200 Kuala Lumpur, Malaysia

²¹ ^bFaculty of Engineering, Universiti Malaysia Sarawak, 94300 Kota Samarahan, Sarawak, Malaysia

²² ARTICLE INFO

²⁶ Keywords:

²⁷ Vortex-induced vibration
²⁸ Vibration energy harvester
²⁹ CFD simulation
³⁰ Streamwise vorticity
³¹ Ensemble empirical mode decompo-
³² sition (EEMD)
³³ Hilbert transform

ABSTRACT

In recent years, the amplitude/frequency responses of an elastically supported circular cylinder-strip plate cruciform have been shown to produce high-amplitude vibrations over a large range of reduced velocities, compared to an isolated circular cylinder. These vibrations are the result of streamwise vortex shedding and are hence in this study, referred to as the streamwise vortex-induced vibration (SVIV). They are commonly studied to exploit their energy harvesting potential. However, amplitude/frequency responses, and the equally important magnitude of lift, are generally presented as a single variable function of quantities that describe flow velocities, such as Reynolds number (Re) or reduced velocity U^* . Despite its utility, this has a side effect of detaching our understanding of the temporal evolution of cylinder displacement and lift from the representative values at each flow velocity. We find such studies scarce and therefore decided to investigate the amplitude and frequency responses of the said cruciform system in the Reynolds number range $1.1 \times 10^3 < Re < 14.6 \times 10^3$ experimentally in an open water channel and numerically using the open source C++ library: OpenFOAM. We decompose the cylinder displacement and lift force time series from our numerical results into Hilbert transform-friendly monotonic functions using the ensemble empirical mode decomposition (EEMD) method. The amplitude/frequency responses suggest the presence of two vibration regimes: the Karman vortex-driven regime when $U^* < 18.2$. The mean phase lag obtained through Hilbert transform points to the existence of an “initial branch”-like state, with a phase lag of ≈ 20 deg. for the streamwise vortex-induced vibration (SVIV) in a narrow region of U^* close to 18.2. Then, the mean phase lag jumps from ≈ 20 deg. to ≈ 110 deg. once $U^* \geq 20.5$, implying transition to some state akin to the “upper branch” of SVIV. The temporal evolution of the instantaneous phase lag shows that SVIV is quasi-periodic up until $U^* = 27.3$. The instantaneous frequency spectrum of lift indicates that Karman vortex shedding continues to leave its trace on the total lift even after the onset of SVIV. Honing into the contribution to the total lift by the Karman and streamwise components of lift reveals that both components possess comparable magnitude between $18.2 \leq U^* \leq 22.7$, while between $25.0 \leq U^* \leq 29.5$, the Karman component contribution is on average twice that of the streamwise component, the power generated by the system can potentially increase by a factor of 2 between $18 < U^* < 23$, and by a factor of 3 when $23 < U^* < 30$.

⁵⁶ 1. Introduction

⁵⁷ Streamwise vortex-induced vibration (SVIV) is a type of vortex-induced vibration (VIV) driven by vortical struc-
⁵⁸ tures whose vorticity vector points in the direction of the free stream. In recent decades, there have been efforts to
⁵⁹ exploit the SVIV phenomenon from cruciform structures for energy harvesting. The literature on this subject can be
⁶⁰ broadly categorised into two groups: how the mechanical properties of the oscillator (e.g., mass ratio, damping, etc.)
⁶¹ affects the amplitude/frequency response of SVIV (Koide et al., 2009, 2013; Nguyen et al., 2012) and how the minutiae
⁶² of the flow field affect the force driving the vibration of the cylinder, i.e. the fluid mechanical aspect of the system

*Corresponding author

 aafkhairi@graduate.utm.my (A. Adzlan); sukri.kl@utm.my (M.S.M. Ali)

ORCID(s): 0000-0003-0290-3185 (A. Adzlan)

63 (Deng et al., 2007; Koide et al., 2017; Zhao and Lu, 2018).

64 In the first focus area, researchers studied some permutation of the following method to convert the vibration into
 65 electrical power. The method consists of a coil and magnet. The coil, which moves with the vibrating cylinder, creates
 66 relative motion against the magnet, which is placed in the hollow of the coil (Koide et al., 2009). While investigating
 67 the system at a Reynolds number in the order of $Re \sim O(10^4)$, Koide et al. (2009) showed that increased damping
 68 due to energy harvesting reduces the maximum vibration amplitude close to a factor of 4. Amplitude reduction due to
 69 increased total damping was also mentioned in Bernitsas et al. (2008); Bernitsas and Raghavan (2008); Bernitsas et al.
 70 (2009). Further investigation in Nguyen et al. (2012) revealed that damping not only affects the amplitude response of
 71 the cylinder but also narrows the synchronisation region between vortex shedding and cylinder vibration. Moreover,
 72 Nguyen et al. (2012) demonstrated a strong coupling between mass ratio and damping in determining both the width
 73 of the synchronisation region and the maximum amplitude response of the cylinder.

74 In the second focus area, investigators turned their attention to the details of the flow where streamwise vortex
 75 shedding occurs. One such study carefully shot motion pictures of the dye-injected flow (Koide et al., 2017) at Reynolds
 76 number in the order of $Re \sim O(10^3)$. A lower Reynolds number (Re) reduces the amount of turbulence in the flow,
 77 allowing a clearer shot of the vortex structures. Their study also highlights the higher level of turbulence produced by
 78 the circular cylinder—strip-plate cruciform in contrast to the twin circular cylinder cruciform, which diminishes the
 79 periodicity of vortex shedding. Although visually enlightening, this and other more qualitative studies contribute little
 80 towards improving our understanding of the relationship between vortex shedding and the resulting lift. Deng et al.
 81 (2007) demonstrated a way to overcome such a shortcoming.

82 In their study, Deng et al. (2007) examined the flow field of a twin circular cylinder cruciform using computational
 83 fluid dynamics (CFD). Their domain stretches $28D$ in the streamwise direction, $16D$ in the transverse direction and
 84 $12D$ in the spanwise direction. They studied an Re range yet another order of magnitude smaller than that studied by
 85 Koide et al. (2017), possibly to get an even clearer visualisation of the vortical structures with less turbulence, and to
 86 ease computational requisites.

87 At a fixed $Re = 150$, streamwise vortices form even at a gap ratio of 2. This result differs quite strikingly from
 88 Koide et al. (2006, 2007), conducted at an Re twice the order of magnitude of Deng et al. (2007), an indication that
 89 the minimum gap ratio needed for the onset of streamwise varies with respect to Re .

90 They also observed that when the gap ratio G , which they denote as L/D in their paper, increases from 3 to 4,
 91 the maximum amplitude of the lift coefficient increases by almost threefold. This can be attributed quite easily to the
 92 current vortex pair shed by the upstream cylinder. The downstream cylinder immediately disturbs the pair shed from
 93 the upstream cylinder when $G = 3$. The lift coefficient increases by about a factor of 3 when this immediate disturbance
 94 diminishes at $G = 4$. The visualisation of three-dimensional (3D) vorticity isocontours enables us to quickly establish

95 this link vis-à-vis the lift coefficient signal. The authors use of CFD made this possible.

96 A similar study in the order of magnitude $\text{Re} \sim O(10^2)$ by Zhao and Lu (2018) particularly highlighted the
 97 immense utility of CFD as a tool to research SVIV or flow around a cruciform in general. They computed the sectional
 98 lift coefficient along the upstream cylinder and the time history of this sectional lift coefficient points towards two
 99 different modes of vortex shedding, namely, parallel and K-shaped. They also paid attention to the local flow patterns
 100 that vary along the length of the upstream cylinder such as the trailing vortex flow, necklace vortex flow and flow in
 101 the small gap (denoted as SG flow). As shown by the discontinuities in the phase angle of the sectional lift coefficient
 102 along the upstream cylinder, we wondered whether the lift coefficient here can be considered due to streamwise vortex
 103 shedding alone, when Karman vortex streamlines were also observed some distance away from the junction of the
 104 cruciform.

105 While we find it persuasive to attribute the frequency/ amplitude modulation of the lift signal in a KVIV system to
 106 the shedding of Karman vortices, one becomes more cautious in doing so solely as the result of streamwise
 107 vortex shedding in an SVIV system. The main reason behind this lies in the fact that the cylinder continues to shed
 108 Karman vortices even after the onset for streamwise vortex shedding and SVIV (Shirakashi et al., 1989). This point
 109 leads us to hypothesise that the lift signal is more appropriately viewed as the streamwise-Karman vortex-induced
 110 composite lift signal. However, we could not find studies that took this viewpoint in their investigation of SVIV and
 111 worked out its implication on power generation.

112 The objectives of this study are thus threefold: (1) to take a closer look at the amplitude and frequency response
 113 of a circular cylinder-strip plate cruciform, especially in U^* ranges where the transition from KVIV to SVIV occurs,
 114 (2) to demonstrate the compositeness of the lift signal of an SVIV system and establish the difference between the lift
 115 signal characteristics in the KVIV and SVIV regime and (3) to shed light on how the contribution from the Karman and
 116 streamwise components of lift changes as we increase U^* after the onset of SVIV and predict how much improvement
 117 in the power generation can be anticipated if we are able to unify the lift amplitude contributions due to Karman and
 118 streamwise vortex shedding. The following §2 details the methodology we employ to conduct this study. We present
 119 and discuss our results in §4, §5, and §6. We describe our conclusions in §7.

120 2. Methodology

121 2.1. Problem geometry

122 The geometrical setup for this study builds on the work of Maruai et al. (2017, 2018) who studied both experimen-
 123 tally and numerically the FIM of a square cylinder with a downstream flat plate. Their simulation results are in good
 124 agreement with their own experiment, and with the experimental results of Kawabata et al. (2013), in the Reynolds
 125 number range $3.6 \times 10^3 < \text{Re} < 12.5 \times 10^3$. This is well within the Reynolds number studied in this work, i.e.

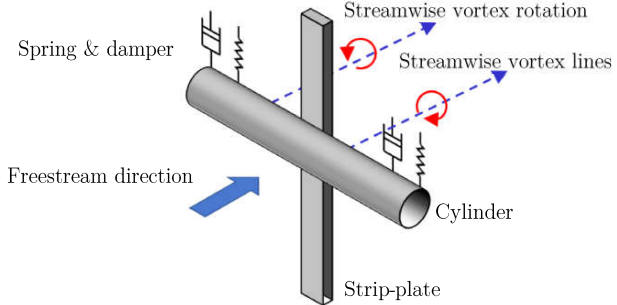


Figure 1: A schematic of the circular cylinder-strip plate cruciform system. Alternate shedding of the streamwise vortices create the alternating lift that drives the vibration of the cylinder.

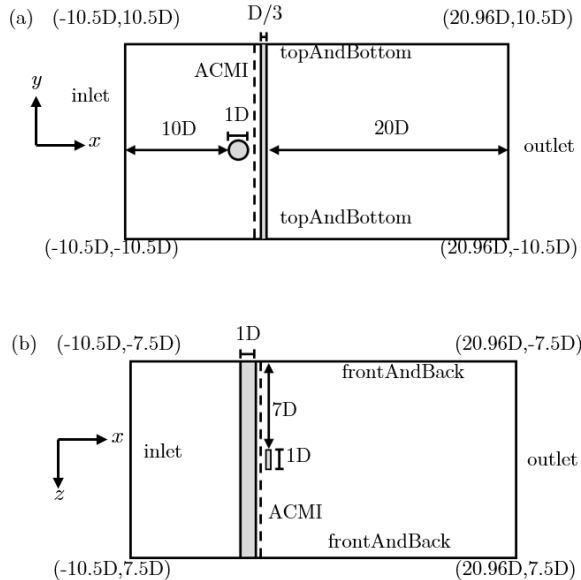


Figure 2: Problem geometry and coordinate system used. (a) shows the side view of the simulation domain (viewed parallel to the freestream) while (b) shows the top view of the simulation domain (viewed perpendicular to the freestream). Note that the gap ratio G between the cylinder and the strip plate is $0.16D$, and the ACMI patch is located midway through the gap, i.e., $0.08D$ downstream from the trailing edge of the cylinder.

$$1.1 \times 10^3 < \text{Re} < 14.6 \times 10^3.$$

Our $x - y$ plane fundamentally follows the dimensions used in Maruai et al. (2017, 2018), except for the cylinder shape, which in this study is circular, and the $20D$ distance to the outlet is measured from the downstream face of the strip-plate. This is shown in Fig. 2. We chose the cylinder-plate gap G to be $0.26D$, as previous works have shown this gap size sustains the highest SVIV amplitude over the widest range of U^* , in comparison to other gap sizes.

As the problem geometry is explicitly three-dimensional (3D), the $x - y$ plane is extruded in the z direction, thus obtaining a 3D domain. As can be seen in Fig. 2, the circular cylinder extends from $z/D = 7.5$ to $z/D = -7.5$, while the strip-plate extends from -10.5 to $y/D = 10.5$. The z -direction extent is set as $z/D = \pm 7.5$ is already more

¹³⁴ than twice the spanwise reach of the streamwise vortex, thus sufficient for the vortices to materialise in our numerical
¹³⁵ solution. To compare, the spanwise extent of the numerical study by Deng et al. (2007), is $z/D = \pm 6$ and the spanwise
¹³⁶ extents of experiments by Nguyen et al. (2012) and Koide et al. (2013) are $z/D = \pm 5$.

¹³⁷ 2.2. Numerical method

¹³⁸ The objectives of our study necessitate the solution of the continuity, and 3D unsteady Reynolds averaged Navier-
¹³⁹ Stokes (3D URANS) equations. We achieve this by using OpenFOAM, an open-source computational fluid dynamics
¹⁴⁰ (CFD) platform written in C++. Specifically, we work to solve the following continuity and URANS equations.

$$\frac{\partial U_i}{\partial x_i} = 0, \quad (1)$$

$$\frac{\partial U_i}{\partial t} + U_j \frac{\partial U_i}{\partial x_j} = -\frac{1}{\rho} \frac{\partial P}{\partial x_i} + \frac{\partial}{\partial x_j} \left(2\nu S_{ij} - \overline{u'_j u'_i} \right). \quad (2)$$

¹⁴¹ The symbols U , x , t , ρ , P , ν , S , and u' are the mean component of velocity, spatial component, time density,
¹⁴² pressure, kinematic viscosity, mean strain rate and the fluctuating component of velocity, respectively. The mean
¹⁴³ strain rate S_{ij} is given by

$$S_{ij} = \frac{1}{2} \left(\frac{\partial U_i}{\partial x_j} + \frac{\partial U_j}{\partial x_i} \right). \quad (3)$$

¹⁴⁴ This study employs the Spalart-Allmaras turbulence model to approximate the Reynolds stress tensor $\tau_{ij} = \overline{u'_j u'_i}$.
¹⁴⁵ This turbulence model has been shown to produce results that agree reasonably well with experiments in similar flow-
¹⁴⁶ induced motion (FIM) studies (Ding et al., 2015a,b). We use the Boussinesq approximation to relate the Reynolds
¹⁴⁷ stress tensor to the mean velocity gradient

$$\tau_{ij} = 2\nu_T S_{ij}, \quad (4)$$

¹⁴⁸ where ν_T represents the kinetic eddy viscosity. ν_T is, in turn, a function of \tilde{v} and f_{v1} , while f_{v1} is a function of χ and
¹⁴⁹ c_{v1} , and χ a function of \tilde{v} and v , as shown in Eq. 5.

$$\nu_T = \tilde{\nu} f_{\nu 1}, \quad (5a)$$

$$f_{\nu 1} = \frac{\chi^3}{\chi^3 + c_{\nu 1}^3}, \quad (5b)$$

$$\chi = \frac{\tilde{\nu}}{\nu}. \quad (5c)$$

150 Here, $\tilde{\nu}$ serves to mediate the turbulence model and dictates how $\tilde{\nu}$ is conserved.

$$\begin{aligned} \frac{\partial \tilde{\nu}}{\partial t} + U_j \frac{\partial \tilde{\nu}}{\partial x_j} &= c_{b1} \tilde{S} \tilde{\nu} - c_{w1} f_w \left(\frac{\tilde{\nu}}{D} \right)^2 \\ &+ \frac{1}{\sigma} \left\{ \frac{\partial}{\partial x_j} \left[(\nu + \tilde{\nu}) \frac{\partial \tilde{\nu}}{\partial x_j} \right] c_{b2} \frac{\partial \tilde{\nu}}{\partial x_i} \frac{\partial \tilde{\nu}}{\partial x_i} \right\} \end{aligned} \quad (6)$$

151 c_{b1} , c_{b2} , and $c_{\nu 1}$ are constant with values 0.1335, 0.622 and 7.1 respectively. c_{w1} is given by

$$c_{w1} = \frac{c_{b1}}{\kappa} + \frac{1 + c_{b2}}{\sigma}, \quad (7)$$

152 where additional constants κ and σ are 0.41 and 2/3 respectively. f_w , on the other hand, is given by

$$f_w = g \left(\frac{1 + c_{w3}^6}{g^6 + c_{w3}^6} \right)^{\frac{1}{6}}. \quad (8)$$

153 Here, $c_{w3} = 2$ while g is given by

$$g = r + c_{w2} (r^6 - r), \quad (9)$$

154 where r is

$$r = \min \left(\frac{\tilde{\nu}}{\tilde{S} \kappa^2 d^2}, 10 \right), \quad (10)$$

155

Additionally, \tilde{S} is

$$\tilde{S} = \Omega + \frac{\tilde{v}}{\kappa^2 d^2} f_{v2}, \quad (11)$$

156 where Ω and d are the magnitude of vorticity and the distance from the mesh nodes to the nearest wall, respectively.

157 Finally, f_{v2} is

$$f_{v2} = 1 - \frac{\chi}{1 + \chi f_{v1}}. \quad (12)$$

158 We solve these equations numerically using the PIMPLE algorithm, which combines the transient solver PISO with

159 the steady-state solver SIMPLE for improved numerical stability.

160 2.3. Dynamic mesh motion

161 In this study, the cylinder in VIV moves perpendicular to the free stream direction. The motion unavoidably
 162 distorts the mesh around it, degrading important mesh metrics such as non-orthogonality and skewness. However, we
 163 can diffuse the mesh deformation to the neighbouring nodes as per the following Laplace equation,

$$\nabla \cdot (\gamma \nabla u) = 0. \quad (13)$$

164 Here, u represents the mesh deformation velocity and γ is displacement diffusion. We chose $\gamma = 1/l^2$, where l is the cell
 165 centre distance to the nearest cylinder edges. We implement the GAMG linear solver with the Gauss-Seidel smoother to
 166 solve Eq. 13. The dynamic mesh algorithm then updates the mesh node positions according to the following equation.

$$x_{\text{new}} = x_{\text{old}} + u \Delta t \quad (14)$$

167 The solver resumes the solution of Eqs. 1 and 2 once the mesh node positions are updated.

168 Another dynamic mesh handling technique used in this study is the arbitrarily coupled mesh interface (ACMI) that
 169 allows non-conforming meshes to slide over another, thus preserving the mesh quality around a moving object. The
 170 tiny gap between the cylinder and strip-plate, limits our ability to diffuse the mesh deformation to the surrounding
 171 space. ACMI is thus implemented at the centre of the gap between the circular cylinder and the strip-plate, as shown in

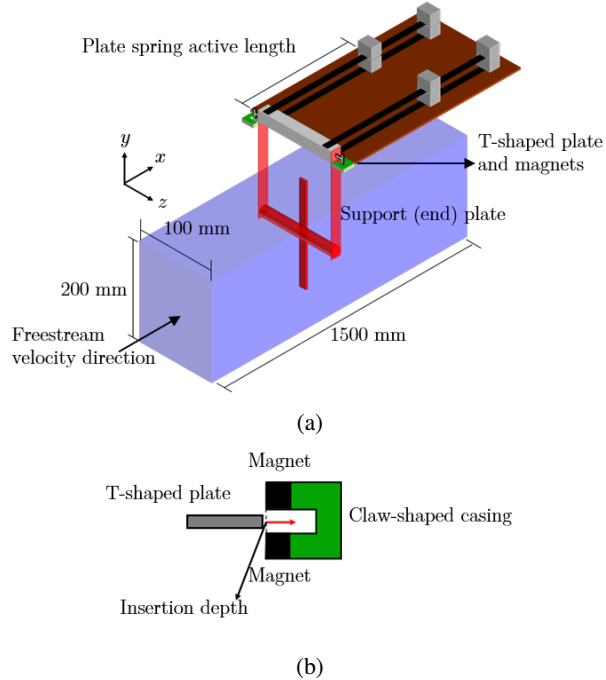


Figure 3: A schematic of our experimental setup. Fig. 3a presents a 3D schematic of the experimental rig while Fig. 3b shows an enlarged schematic of the damping system.

172 Fig. 2, to circumvent this problem. This method has been successfully implemented in the works of Ding et al. (2015b);
 173 Zhang et al. (2018), preserving the quality of their mesh and controlling their Courant-Friedrichs-Lowy (CFL) number.

174 2.4. Open flow channel experiment

175 One of the aims of this work is to study the transition between Karman and streamwise vortex-induced vibration.
 176 Therefore, we set up an experimental rig to study the VIV motion in the vicinity of U^* where the vortex-induced
 177 vibration transitions from Karman to streamwise vortex driven. To this end, we constructed a closed-loop open channel
 178 circuit based on the water tunnel used by Nguyen et al. (2012), shown in Fig. 3. The cross-section of out test section
 179 is a rectangle of with 100 mm from the bottom of the test section throughout its length of 1500 mm.

180 The system for providing elastic support and damping to the circular cylinder follows closely those used by Kawa-
 181 bata et al. (2013) and Koide et al. (2013, 2017), which can be summarised as follows. The stiffness coefficient k of
 182 the plate spring is determined through a simple weight versus displacement test (Sun et al., 2016), at various active
 183 lengths of the spring. This provides a calibration curve of stiffness coefficient, k against plate spring length, l . We can
 184 then adjust the length of the plate spring to obtain the desired value for k .

185 On the other hand, the damping of the system is adjusted using T-shaped aluminium plates fixed at either end of
 186 the cylinder endplate, and a pair of neodymium magnets contained in a claw-shaped casing. The further the T-shaped
 187 plate is pushed into the opening of the claw, the denser the magnetic field it needs to cut through during motion, thus

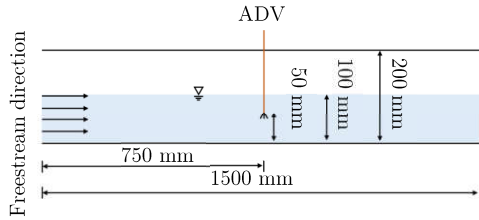


Figure 4: Side view of the open flow channel, in schematic form. Also, key dimensions of the experimental setup. The acoustic Doppler velocimeter (ADV) is placed at the same location where the cylinder is located during experimental runs.

188 dissipating more energy. We then calibrate the damping produced at various depths at which the T-shaped plate is
 189 pushed into the casing, via free-decay tests of the cylinder in still water. The procedure for conducting free-decay tests
 190 are detailed in Raghavan (2007).

191 Flow inside the open channel is driven by a 3.728 kW (5 hp) centrifugal pump, controlled using a voltage controller.
 192 The input voltage for the centrifugal pump is calibrated against the centreline velocity of the test section, 750 mm from
 193 the inlet, i.e. mid-length of the test section. We show this schematically in Fig. 4. Here, we define the centreline of the
 194 test section as the line 50 mm from the bottom and 50 mm from either of the sidewalls of the test section. We placed
 195 the cylinder in the same position during experimental runs.

196 The centreline velocity U_{cent} is measured using an acoustic Doppler velocimeter (ADV), sampling at 200 Hz.
 197 The resulting calibration curve is applicable for determining U_{cent} at input voltages $30 < V_{\text{in}}(\text{V}) < 100$. We measured
 198 the turbulence intensity along the centreline to be about 5%.

199 We obtained the time history for cylinder displacement by using a video camera pointed normal to the cylinder
 200 endplate. We placed a visual marker on the endplate, and the motion of the marker captured by the camera is analysed
 201 using *Tracker*: a motion analysis tool built on the Open Source Physics Java framework.

202 To validate our experimental setup, we tuned to the best of our ability our experimental parameters to the val-
 203 ues used by Koide et al. (2013) and test whether we can replicate their results. The following table summarises the
 204 parameters in lieu of that paper.

Table 1
Summary of experimental parameters in contrast to those used in the experimental work of Koide et al. (2013).

| | Current study | Koide et al. (2013) |
|--|---------------|---------------------|
| Cylinder diameter, D (m) | 0.01 | 0.01 |
| Cylinder length, l_{cylinder} (m) | 0.09 | 0.098 |
| Strip-plate width (m) | 0.01 | 0.01 |
| Strip-plate length (m) | 0.1 | 0.1 |
| Effective mass, m_{eff} (kg) | 0.162 | 0.174 |
| Logarithmic damping, δ | 0.178 | 0.24 |
| Scruton number, Sc | 9.94 | 7.74 |
| System natural frequency, f_n (Hz) | 4.42 | 4.4 to 4.79 |

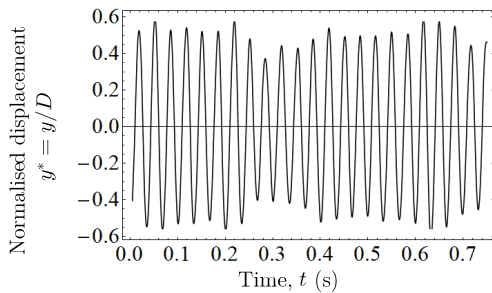


Figure 5: A sample of the time history for cylinder displacement from a test run of our experimental setup. the value of $U^* = 22.7$

We conducted an experiment at $U^* = 22.7$, a value that falls in the SVIV regime, and show a sample of the normalised displacement time series in Fig. 5. Computing the statistics of the normalised displacement $f^* = f_{\text{cyl.}}/f_n$ of the cylinder from several runs gave us a value of $y^* = 0.33 \pm 0.03$ and $f^* = 1.03 \pm 0.04$. Koide et al. (2013) obtained $y^* = 0.32$ and $f^* = 1.09$ under a similar U^* condition. We thus take this fairly successful reproduction of the results of Koide et al. (2013) as an indication of readiness for further data collection.

3. Numerical setup validation

3.1. Simple grid independency study

Numerical solutions of actual, continuous physical phenomena contain errors, or uncertainties, due to temporal and spatial discretisation. Reliance on the numerical method of investigation puts the responsibility on the user to minimise and justify the magnitude of error introduced in the solution.

While CFD users usually point towards their low Courant-Friedrichs-Lowy number to substantiate their claim of temporal convergence for their numerical solutions, researchers demonstrate the spatial convergence of their solution through either one of these methods. First, by solving the governing equations on several grids, each grid being a finer version of the previous one and showing that the quantities of interest are approximately the constant on all grids tested. One then chooses the mesh with a medium resolution to use in the subsequent data collection (Wu, 2011; Ding et al., 2013, 2015a, 2019).

3.2. Grid independency study via Richardson extrapolation and grid convergence index

Like the first, the second method solves the governing equations on successively finer grids. However, instead of arguing that one obtains similar results on all the grids, the investigator checks whether the quantities of interest tend towards value, as one solves the governing equation on successively finer grid resolutions (Richardson and Gaunt, 1927; Stern et al., 2001). This method, of checking for convergence pays attention not only on the presumed converged value but also on the trend of convergence. Literature that employ this method impose a monotonic convergence condition

227 (Stern et al., 2001; Mat Ali et al., 2011; Ali et al., 2012; Maruai et al., 2018) on their quantities of interest, adding an
228 extra layer of confidence in the final form of their spatial discretisation.

229 Additionally, this method allows for a quantitative description of the degree of convergence through the grid conver-
230 gence index (GCI). Let $f_1, f_2, f_3, \dots, f_n$ denote the quantity of interest obtained from several grids. A larger subscript
231 indicates a coarser grid, this f_1 denotes the finest while f_n denotes the coarsest grid. Let the difference between suc-
232 cessive solutions be $\epsilon_{2,1}, \epsilon_{3,2}, \epsilon_{4,3}, \dots, \epsilon_{n,n-1}$, where $\epsilon_{2,1} = f_2 - f_1, \epsilon_{3,2} = f_3 - f_2$ and so on. Then, the GCI is defined
233 as

$$\text{GCI}_{i+1,i} = F_s \frac{|\epsilon_{i+1,i}|}{f_i(r^p - 1)} \times 100\%, \quad (15)$$

234 where F_s , f_i and r^p denotes the safety factor ($= 1.25$), quantity of interest and the refinement ratio, r , between successive
235 grids raised to the order of accuracy of the series of solution, p . We refer the reader to Stern et al. (2001); Langley
236 Research Centre (2018) for a more detailed discussion on r^p .

237 We can estimate what the solution approaches as the grid size approaches zero by using the p^{th} method. Briefly,
238 we compute the generalised Richardson extrapolation of the quantity of interest as follows.

$$f_{\text{RE}} = f_1 + \frac{f_1 - f_2}{r^p - 1}, \quad (16)$$

239 where f_{RE} is the Richardson extrapolation of the quantity of interest. Using f_{RE} to estimate the limit of the monoton-
240 ically convergent series of f_i , we can determine the percentage difference of our solution on our finest grid from this
241 limit as

$$E_i = \frac{f_i - f_{\text{RE}}}{f_{\text{RE}}} \times 100\%. \quad (17)$$

242 Table 2 summarises the result of our grid independency study for the SVIV reduced velocity of $U^* = 22.7$.
243 We identified three quantities central to the investigation of fluid-structure phenomena, especially the flow-induced
244 vibration of a circular cylinder. They are the vibration amplitude, vibration frequency and lift coefficient of the cylinder.
245 We solve the governing equations on three grids which are numbered 1 for the finest, 2 for the medium and 3 for the
246 coarsest, shown in Fig. 6. If we let v_i be the volume of the i^{th} cell in the grid, then, the average cell size is

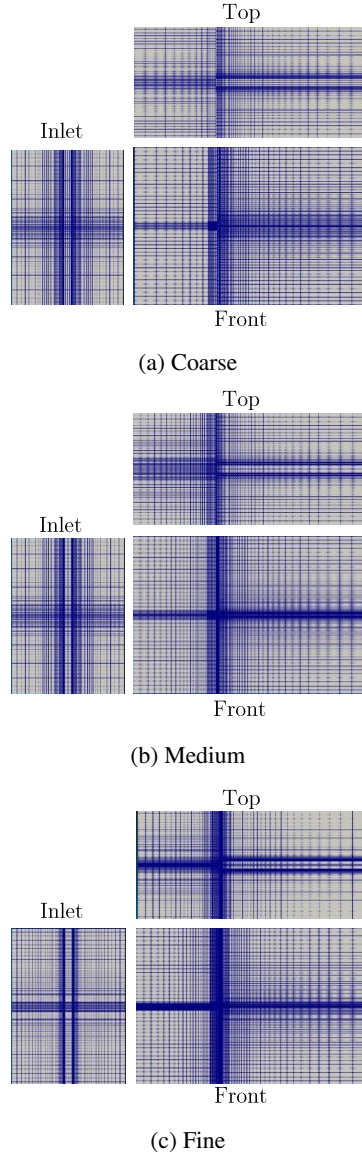


Figure 6: Three meshes used in the grid convergence study. Figs. 6a, 6b and 6c show the coarse, medium and fine meshes viewed perpendicular to three main viewing positions: from the inlet, the top and the front, which is looking directly at the cylinder end.

$$h = \frac{1}{N} \left[\sum_{i=1}^N v_i \right]^{1/3}, \quad (18)$$

247 and the normalised average cell size is hence

$$h/D = \frac{1}{ND} \left[\sum_{i=1}^N v_i \right]^{1/3}. \quad (19)$$

248 Both y_{RMS}^* and Cl_{RMS} starts at an initial value smaller than their Richardson extrapolations, f_{RE} , before approaching
 249 it as we decrease the average cell size, h . This similar trend can perhaps be attributed to the causal relationship between
 250 the lift coefficient and vibration amplitude. The lift drives and sustains the vibration, hence a small lift produces a small
 251 vibration, and when the lift amplitude becomes higher, so too does the vibration amplitude. The vibration frequency,
 252 on the other hand, starts at a value larger than its f_{RE} before approaching f_{RE} .

253 The quantity Cl_{RMS} experiences the most significant drop in GCI as we refine the grid. The GCI is close to one-
 254 third (30.92%) as we refine the grid from coarse to medium with a refinement ratio of 1.376. The refinement ratio is
 255 calculated by dividing the number of cells in one grid with the next one down the refinement line. Following the grid
 256 numbering convention explained previously, dividing the number of cells in the fine grid (grid 1) with the number of
 257 cells in the medium grid (grid 2) gives us the refinement ratio from medium to fine, or $r_{2,1}$. Similarly, dividing the
 258 number of cells in the medium grid (grid 2) with the number of cells in the coarse grid (grid 3) gives us the refinement
 259 ratio from coarse to medium, or $r_{3,2}$. We can generalise this to n -number of grids as follows.

$$r_{i+1,i} = \frac{S_{\text{grid},i+1}}{S_{\text{grid},i}}, \quad (20)$$

260 where $S_{\text{grid},i}$ denotes the total number of cells in the i^{th} grid. The GCI of Cl_{RMS} drops further to 1.63% as the mesh is
 261 refined more with a refinement ratio of 1.304.

262 The GCI for y_{RMS}^* also drops by one order of magnitude as can be seen by comparing $\text{GCI}_{3,2}$ with $\text{GCI}_{2,1}$. Again,
 263 this similar trend of improvement points to the causal relationship between lift and displacement of the cylinder. The
 264 GCI for f^* , however, drops by approximately a factor of 6 instead of one order of magnitude, unlike the GCIs of y_{RMS}^*
 265 and Cl_{RMS} .

266 We provide visual representations of the convergent Cl_{RMS} , y_{RMS}^* and f^* series in Figs. 7, 8 and 9. Note how the
 267 quantity of interest is very close to its Richardson extrapolation at the fine grid (grid 1) for all Cl_{RMS} , y_{RMS}^* and f^* .
 268 This implies that the fine grid already provides adequate spatial discretisation for the problem we are studying, and
 269 further refinements, while able to nudge our solutions even closer to the limit that is the Richardson extrapolation, may
 270 not be optimal in terms of usage of computational resources. Values of y_{RMS}^* and f^* at the fine grid already fall within

Table 2

Summary of grid independency study.

| Parameter/ metric | CI_{RMS} | $y_{\text{RMS}}^* = y^*/D$ | $f^* = f_{\text{cyl.}}/f_n$ |
|---|--------------------------|----------------------------|-----------------------------|
| f_{RE} | 0.262 | 0.369 | 0.969 |
| f_1 | 0.2598 | 0.3687 | 0.9695 |
| f_2 | 0.2430 | 0.3588 | 0.9740 |
| f_3 | 0.0805 | 0.2374 | 1.0220 |
| $ \epsilon_{2,1} $ | 0.02 | 0.01 | 0.004 |
| $ \epsilon_{2,1} $ | 0.16 | 0.12 | 0.48 |
| $R = \epsilon_{2,1} / \epsilon_{2,1} $ | 0.10 | 0.08 | 0.094 |
| $\text{GCI}_{3,2}$ | 30.92 | 6.00 | 0.64 |
| $\text{GCI}_{3,2}$ | 1.63 | 0.52 | 0.10 |

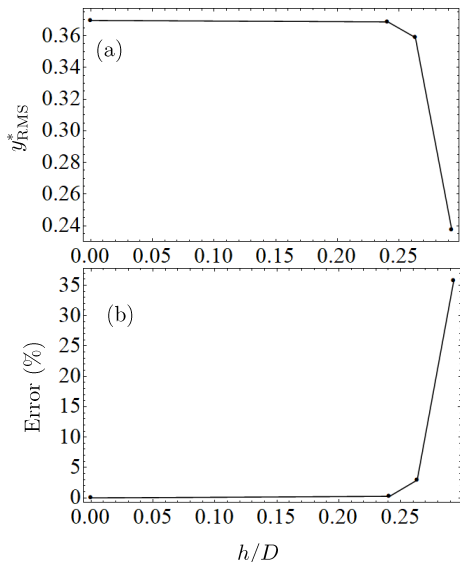


Figure 7: The convergence diagram for y_{RMS}^* . Fig. 7a shows how y_{RMS}^* converges close to the Richardson extrapolation value while Fig. 7b shows how the error (difference between the value obtained from a particular mesh and the Richardson extrapolation) decreases with decreasing grid spacing.

experimental uncertainty as evidenced by our measurement in §2.4 and the work by Koide et al. (2013). Hence, all succeeding numerical data are gathered from the fine grid.

4. Single plate amplitude and frequency response

4.1. Amplitude response

We compared our experiment and numerical results with those from Koide et al. (2013) and Nguyen et al. (2012) in Fig. 10. Figure 10a shows the amplitude response of our single plate experiment and simulation. We use the root-mean-square value of the cylinder displacement to represent the amplitude responses instead of the maximum displacement. The reason for this is twofold: first, using y_{RMS}^* facilitates comparison of data with Nguyen et al. (2012) and Koide

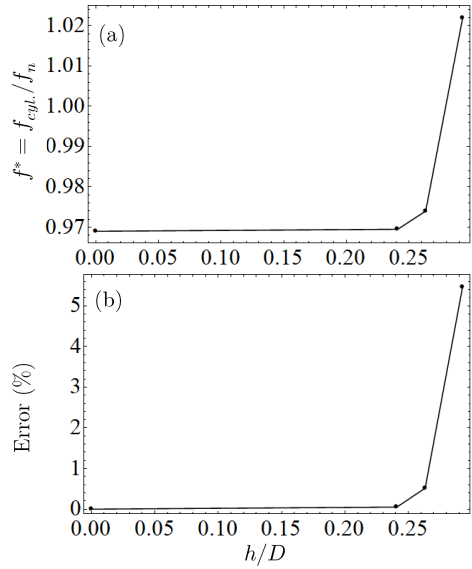


Figure 8: The convergence diagram for f^* . Fig. 8a shows how f^* converges close to the Richardson extrapolation value while Fig. 8b shows how the error (difference between the value obtained from a particular mesh and the Richardson extrapolation) decreases with decreasing grid spacing.

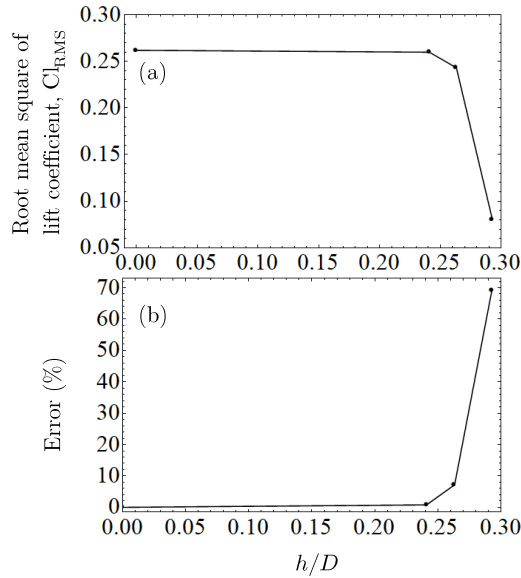


Figure 9: The convergence diagram for Cl_{RMS} . Fig. 9a shows how Cl_{RMS} converges close to the Richardson extrapolation value while Fig. 9b shows how the error (difference between the value obtained from a particular mesh and the Richardson extrapolation) decreases with decreasing grid spacing.

et al. (2013), who also used y_{RMS}^* in their work. Second, because the cylinder displacement is an intermediate quantity for the estimation harnessed power (Maruai et al., 2017, 2018), the usage of root-mean-square of cylinder displacement gives a preview of mean harnessed power, once the vibration is converted into alternating current.

There is virtually no vibration for both our experiment and simulation when $U^* < 18$, except for a small peak close

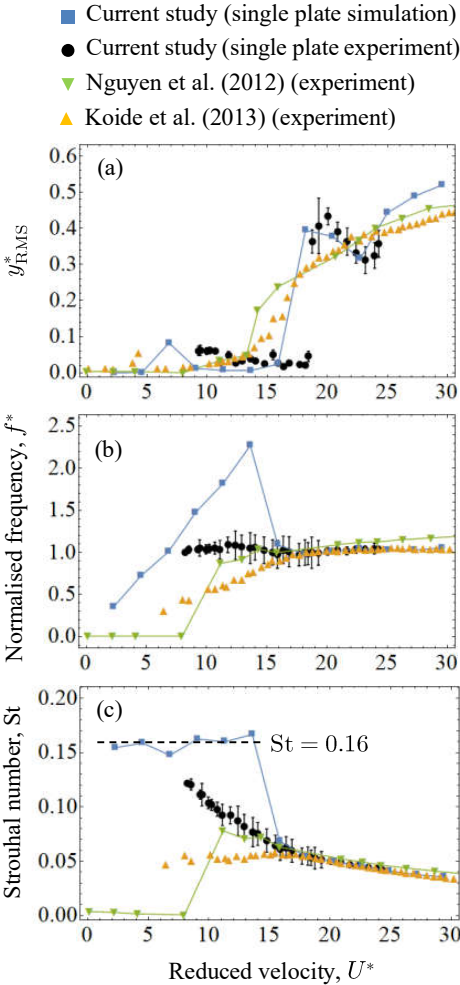


Figure 10: The amplitude and frequency response of our cruciform system, in lieu of results from Nguyen et al. (2012); Koide et al. (2013). Fig. 10a shows the amplitude response using y_{RMS}^* , Fig. 10b the frequency response using f^* and Fig. 10c also the frequency response, but using the Strouhal number of vibration.

to 0.1 at $U^* \approx 7$. We attribute this peak to the upper branch of KVIV, which still exists, although suppressed due to the cruciform configuration of the system (Shirakashi et al., 1989; Nguyen et al., 2012). However, when U^* exceeds 18, we observe a sudden jump in U^* right up to about 0.4, for both our experiment and simulation. This we attribute to the formation of the streamwise vortices that drive SVIV.

After the inception of SVIV, the value for y_{RMS}^* drops down to approximately 0.3, before recovering to a value that is close to what was observed by Nguyen et al. (2012) and Koide et al. (2013). This sudden jump followed by a gradual drop and a gradual rise in y_{RMS}^* was not found in the works of Nguyen et al. (2012) nor Koide et al. (2013), even though their experimental parameters are reasonably close to what we use in both our experiment and simulation.

We, therefore, attribute this difference to the higher turbulence level set in our work. The turbulence level in the works of Nguyen et al. (2012), for example, was < 2.8% throughout their range of Reynolds number. Instead, the

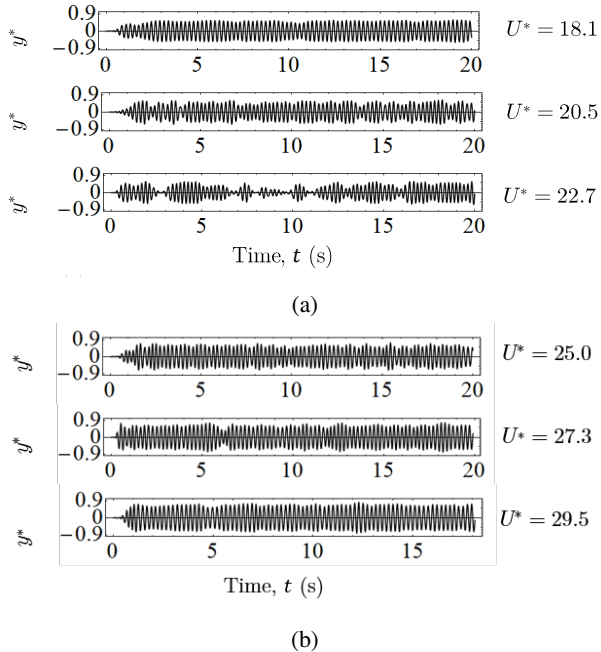


Figure 11: The time series of cylinder displacement between $18 < U^* < 20$. Fig. 11a groups the cylinder displacement signal between $18 < U^* < 23$, where there seems to be an increase in intermittency in the displacement signal, while Fig. 11b groups the cylinder displacement signal between $25 \leq U^* < 30$, where the intermittency in the displacement signal vanishes.

initial turbulence level in our setup, both experimental and numerical, is approximately double that value. Because of this, the turbulence amplification due to the onset of streamwise vortices (Zhao and Lu, 2018) — especially for a circular cylinder-strip plate cruciform (Koide et al., 2017) — is also higher compared to the experiments of Nguyen et al. (2012) and Koide et al. (2013). This higher compound turbulence warps the dominant vortical structure and introduces an increasing amount of intermittency to the lift signal, and by extension, to the displacement time history of the cylinder.

One can simply inspect the error bars within $18 < U^* < 23$ in Fig. 10a to verify the greater sample dispersion within that range of U^* . This intermittency ultimately vanishes as the dominant vortical structures become sufficiently stable to retain enough periodicity in its formation. Our numerical results also seem to support this argument, as evidenced by the time history of U^* within $18 < U^* < 30$ in Fig. 11. There exists a distinct increase in intermittency for the time histories in Fig. 11a, that disappears once $U^* > 23$ as can be seen in Fig. 11b.

We see these as grounds for further study on streamwise vortex shedding onset, perhaps from the perspective of transition from convective to absolute instability. However, such studies are more commonly done under low Reynolds number conditions (Wang et al., 2019; Li et al., 2019) to ease the isolation of the phenomenon and is therefore out of the scope of this study.

308 **4.2. Frequency response**

309 Figure 10a compares the frequency responses of our experiment and numerical results with those in Nguyen et al.
 310 (2012) and Koide et al. (2013). We use the normalised frequency f^* in Fig. 10b and the vibration Strouhal number in
 311 Fig. 10c to aid comparison between the results. In our experiments, the value for f^* always fall close to unity. However,
 312 if we inspect the size of the error bars, we observed a range of U^* where there exists a higher degree of variance in
 313 the sample measurements between $13 < U^* < 20$. The reason for this lies in $13 < U^* < 20$ coinciding with the
 314 desynchronization region of the KVIV regime up to $U^* < 18$, and then overlaps with the intermittent vibration regime
 315 up to $U^* < 20$. Within these two regimes, the cylinder displacement time history — from which f^* is calculated
 316 — varies considerably in amplitude and periodicity, resulting in larger error bars. In Fig. 10c we can see the overall
 317 trend being more similar to the results of Koide et al. (2013) rather than Nguyen et al. (2012), which is likely due to
 318 a higher similarity between our experimental setup with that of Koide et al. (2013), most striking in terms of the gap
 319 ratio $G = g/D$, which is the same.

320 Our numerical results exhibit a significantly different trend, but only up to $U^* < 17$. We observe in Fig. 10b that
 321 the vibration frequency of the cylinder increases linearly, even past $U^* = 7$, which is the upper branch of the KVIV
 322 regime. Converting f^* into Strouhal number reveals that the cylinder is vibrating close to the Karman frequency of
 323 the system. The Karman frequency of a smooth, fixed circular cylinder refers to the shedding frequency of Karman
 324 vortices in its wake. An empirical relationship with Reynolds number exists for $250 < \text{Re} < 2 \times 10^5$, which is the
 325 following Blevins (1990).

$$\text{St} = 0.198 \left(1 - \frac{19.7}{\text{Re}} \right) \quad (21)$$

326 The values we get using Eq. 21 are nearly constant about 0.19 for $U^* < 15$. The slight discrepancy from our
 327 Strouhal number mean (≈ 0.16) in the $U^* < 15$ range can be ascribed to us studying a cruciform structure instead of
 328 the smooth circular cylinder upon which Eq. 21 was originally based (Blevins, 1990).

329 The experimental studies benchmarked in Fig. 10 quite possibly were simply unable to observe this phenomenon
 330 due to insufficient sensitivity in the equipment used to measure the cylinder displacement. The lowest y_{RMS}^* recorded
 331 in our simulation within $7 < U^* < 15$ was in the order of 10^{-5} m (10 microns). A numerical study has no problem
 332 recording vibration of this order as the precision of the numerical solution is only limited by the processor architecture.
 333 Experimental work, however, requires not only the sensitivity but also the isolation from the background noise that
 334 forces the cylinder to vibrate close to the natural frequency of the system f_n (Nguyen et al., 2012), hence overpowering
 335 this minimal amplitude vibration. Once streamwise vortices form, their shedding and cylinder vibration synchronises

³³⁶ close to f_n , thus locking the normalised vibration frequency back to $f^* \approx 1$.

³³⁷ 5. Temporal evolution of the lift coefficient

³³⁸ Alternating lift drives the cylinder vibration during VIV. Despite this central position in determining the temporal
³³⁹ stability of the amplitude and frequency responses, most studies in the SVIV literature dealt with the lift (coefficient) as
³⁴⁰ if it is only a function of flow velocity, U or reduced velocity, U^* (Kawabata et al., 2013; Koide et al., 2013; Hemsuwat
³⁴¹ et al., 2018). We believe that parties interested in the quality of power harnessed from flow around a cruciform should
³⁴² give similar attention to the transient nature of SVIV as they did for the global characteristics of the flow such as the
³⁴³ root mean squares of cylinder displacement, lift coefficient, and dominant frequency through fast Fourier transform
³⁴⁴ (FFT). We think that this is especially the case for the lift signal, to better gauge the room for improvement in future
³⁴⁵ iterations of the system.

³⁴⁶ 5.1. Ensemble empirical mode decomposition and Hilbert transform

³⁴⁷ To obtain a clearer picture of the temporal characteristics of the lift and cylinder displacement signals, we decided
³⁴⁸ to employ the ensemble empirical mode decomposition (EEMD) method (Huang et al., 1998; Wu and Huang, 2008)
³⁴⁹ on the signals, and compute their instantaneous phase lag, frequency and amplitude using the Hilbert transform.

³⁵⁰ The Hilbert transform (HT) has been used in the past to study the instantaneous phase and frequencies of KVIV
³⁵¹ (Khalak and Williamson, 1999). However, the signal must be monochromatic if we are to obtain a physically mean-
³⁵² ingful result after applying HT. EEMD is a way to pre-process the signal and get components that (1) have zero mean,
³⁵³ and (2) have an equal number of extrema and zero crossings, or they differ only by one. Functions that fulfil these
³⁵⁴ criteria are called intrinsic mode functions (IMF), and they guarantee a physically meaningful result to HT (Gumelar
³⁵⁵ et al., 2019; Zhou et al., 2019). Unlike Fourier transform, which is an analytical method of signal decomposition based
³⁵⁶ on circular functions in the complex plane, EEMD is algorithmic, and the processes undertaken can be summarised as
³⁵⁷ follows.

³⁵⁸ Produce 150 white noise signals of length equal to the original signal and amplitude equal to 0.2 of the standard
³⁵⁹ deviation of the original signal. Then, add to the set of white noises the original signal – creating 150 variations of
³⁶⁰ the original signal. Following that, we apply the empirical mode decomposition (EMD) algorithm on each of the 150
³⁶¹ signals. The EMD algorithm is summarised below.

- ³⁶² 1. Construct the envelope of the signal by connecting all maxima/minima with cubic splines.
- ³⁶³ 2. Find the local mean of the envelope for the span of the data.
- ³⁶⁴ 3. Find the difference between the local mean and the original data.
- ³⁶⁵ 4. Repeat steps 1 and 2 on the difference in 3 for ten times (Wu and Huang, 2008).

366 The steps above produce a set of intrinsic mode functions or IMFs for each of the 150 variations of the original
 367 signal. Then, we average the first IMF component from each of the decomposed original signal variations, to obtain
 368 the first EEMD IMF C_1 of the original signal. We do the same for the second, third, until the n^{th} component for each
 369 of the 150 original signal variations, thus obtaining C_2, C_3, \dots, C_n .

370 To compute the phase lag between lift coefficient Cl and normalised cylinder displacement y^* , we select the com-
 371 ponent with the highest correlation to the original signal, to represent the original signal. The phase lag, instantaneous
 372 frequency, and instantaneous amplitude of the original signal is subsequently computed by taking the constructing an
 373 analitical signal $z(t)$ from C_1, C_2, \dots, C_n by taking the Hilbert transform of the IMF H_i ,

$$H_i(t) = \frac{1}{\pi} \text{PV} \int \frac{C_i(\tau)}{t - \tau} d\tau, \quad (22)$$

where PV denotes the Cauchy principal value, and then constructing the analitical signal as follows.

$$z(t) = C_i(t) + iH_i(t) \quad (23)$$

374 Note that i in Eq. 23 is the complex number.

375 We refer the reader interested in the details of EEMD and Hilbert transform, also collectively known as the Hilbert-
 376 Huang transform (HHT), to the following excellent texts on the subject (Huang and Attoh-Okine, 2005; Huang, 2014).

377 5.2. Phase lag in the KVIV regime ($U^* < 14$)

378 At reduced velocities $U^* = 2.3$ and 4.5 , the phase lags ϕ (deg.) between Cl and U^* are practically zero. The
 379 characteristic IMFs of Cl and y^* at $U^* = 4.5$ exemplifies this trend, as showcased in Fig. 12. The characteristic IMFs
 380 are the EEMD components of Cl and y^* that has the highest correlation with the original y^* signal. The trend that one
 381 notices in Fig. 12 is similar to what was observed in Khalak and Williamson (1999), a study that also employs the
 382 Hilbert transform to obtain the instantaneous phase, albeit without EEMD. Both Cl and y^* are in phase with each other
 383 and the normalised dominant frequency of the lift coefficient $f_{\text{Cl}}^* = f_{\text{Cl}}/f_n$ (Fig. 12c) falls about one quarter short of
 384 the system natural frequency f_n .

385 Once we enter the upper branch of KVIV at $U^* = 6.8$, ϕ jumps to approximately 110 deg. This jump in ϕ is
 386 characteristic of the transition to the upper branches as also observed by Maruai et al. (2018), among others. Both Cl
 387 and y^* signals are visibly very periodic, and the dominant frequency of Cl , i.e. f_{Cl}^* , is ≈ 1 , as one can verify in Fig.
 388 13c.

389 As we increase U^* even further up to $U^* < 14$, we see a similar trend for all $U^* = 9.1, 11.4, 13.6$ examined: the

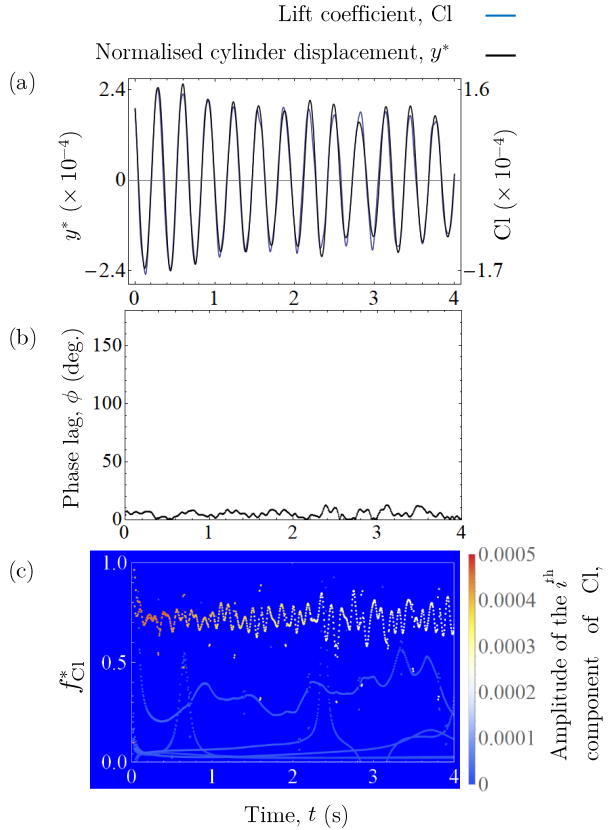


Figure 12: Temporal analysis of the lift coefficient and normalised cylinder displacement signal at $U^* = 4.5$. We show the lift coefficient and normalised cylinder displacement signal side by side in Fig. 12a, present the temporal evolution of the phase lag ϕ of Cl in Fig. 12b and show the temporal evolution of the instantaneous frequency of the lift coefficient signal in Fig. 12c. The blue line in Fig. 12a represents the lift coefficient signal, while the black line represents the normalised cylinder displacement.

390 signal of Cl and y^* are both qualitatively very periodic, the phase lag is very close to 180 deg., and the dominant Cl
 391 frequency increases linearly in a manner that the Strouhal number of Cl is always ≈ 0.16 on average. We present a
 392 sample of the (1) Cl and y^* signals, (2) ϕ , and (3) f_{Cl}^* in the $6.8 < U^* < 14$ range in Figs. 14a, 14b and 14c respectively.
 393 The sample is taken from the numerical results at $U^* = 13.6$, and it is characteristic of a KVIV system in the lower
 394 branch.

395 5.3. Transition to SVIV ($15.9 < U^* < 18.2$)

396 Previously in the $U^* < 14$ regime, we observed that the temporal profile of both Cl and y^* are very similar to each
 397 other, except that Cl leads y^* by a certain amount. This similarity in profile supports the assertion that the vibration
 398 within $U^* < 14$ is driven exclusively by the shedding of Karman vortices, which brings the onset of the alternating lift.
 399 By extension, one might expect a similar profile between Cl and y^* even when streamwise vortices drive the vibration.
 400 However, this does not seem to be the case.

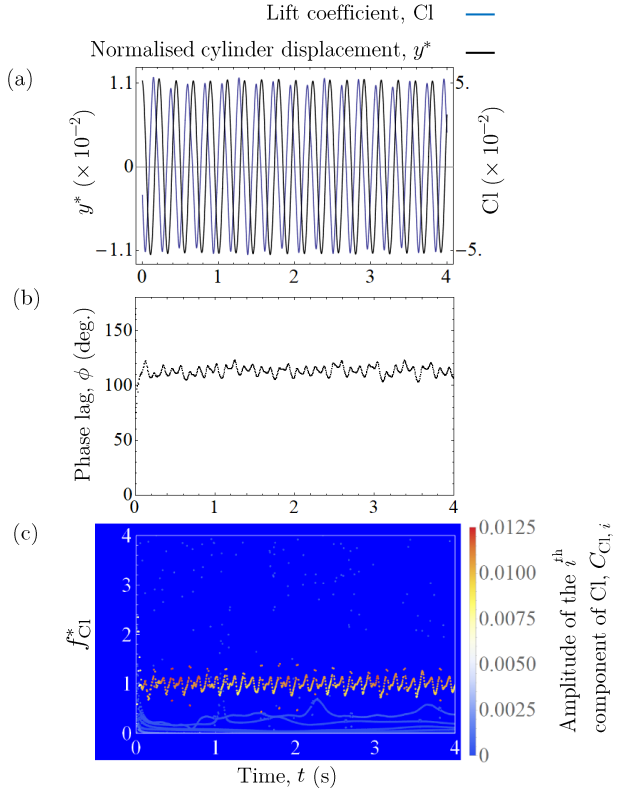


Figure 13: Temporal analysis of the lift coefficient and normalised cylinder displacement signal at $U^* = 6.8$. We show the lift coefficient and normalised cylinder displacement signal side by side in Fig. 13a, present the temporal evolution of the phase lag ϕ of Cl in Fig. 13b and show the temporal evolution of the instantaneous frequency of the lift coefficient signal in Fig. 13c. The blue line in Fig. 13a represents the lift coefficient signal, while the black line represents the normalised cylinder displacement.

Once we reach $U^* = 15.9$, we observe that it has become difficult to argue that the profile of y^* is just a lagged version of the profile of Cl . This is shown in Fig. 15a, with the enlarged version in Fig. 15b. The profile of Cl looks like the result of several superimposed signals, which one can almost distinguish from the presence of two types of maxima at two different amplitude heights. We put a red dashed line and a red dashed-dot line in Fig. 15b as visual cues indicating the two amplitude heights. Decomposing the lift coefficient signal using EEMD reveals partial evidence supporting the superimposed (compound) signal hypothesis.

Once we have decomposed the signal using EEMD, we replot Fig. 15a using the component of Cl with the highest correlation to the original y^* signal and present the comparison in Fig. 16a. To represent y^* in Fig. 16a, we again chose its IMF component with the highest correlation to the original y^* signal, as we have done in Figs. 12, 13, and 14. One can clearly see that the part of Cl signal responsible for driving the vibration at $U^* = 15.9$ is embedded in the original Cl signal, and decomposition via EEMD managed to recover this signal whose profile is indeed similar to the profile of the characteristic IMF of y^* , except that it leads y^* on average by approximately 150 deg. (Fig. 16b). This decline from $\phi \approx 180$ deg. at reduced velocities $6.8 < U^* < 14$, to $\phi \approx 150$ deg. at $U^* = 15.9$ is quite sizeable,

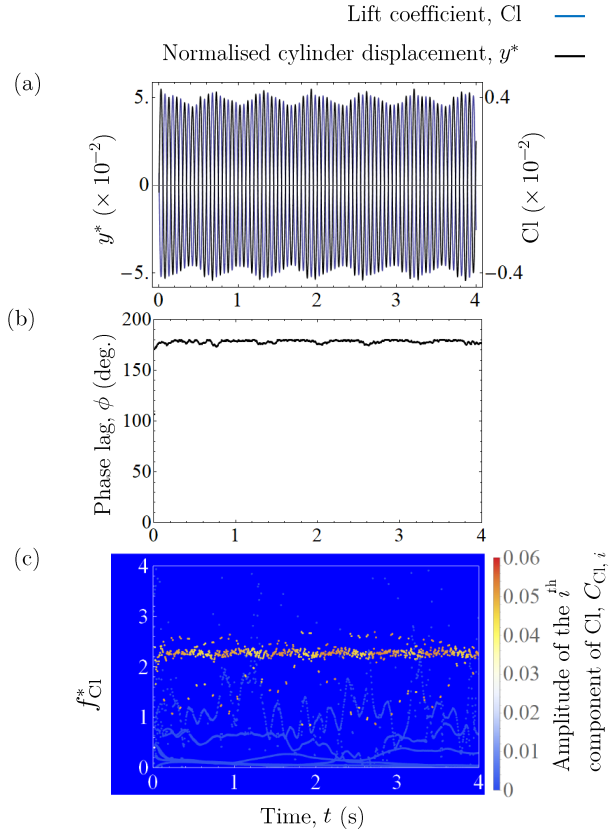


Figure 14: Temporal analysis of the lift coefficient and normalised cylinder displacement signal at $U^* = 13.6$. We show the lift coefficient and normalised cylinder displacement signal side by side in Fig. 14a, present the temporal evolution of the phase lag ϕ of Cl in Fig. 14b and show the temporal evolution of the instantaneous frequency of the lift coefficient signal in Fig. 14c. The blue line in Fig. 14a represents the lift coefficient signal, while the black line represents the normalised cylinder displacement.

suggesting a fundamental change in flow dynamics, particularly in terms of vortical structure.

Inspecting the HHT spectrogram in Fig. 16c reveals two dominant bands in the frequency domain. The first one, marked with a white continuous rectangular box, is the instantaneous frequency for the IMF component of lift shown in Fig. 16a, and its mean frequency lies close to the natural frequency of the system ($f_{Cl}^* \approx 1$). There is; however, a second band of the frequency with nearly similar amplitude around $f_{Cl}^* \approx 3.3$, marked with a white dashed rectangular box. Computing the Strouhal number from this frequency returns a value of $St = 0.20$, which is very close to the Strouhal number for Karman vortices as predicted by Eq. 21 at the Reynolds number equivalent to $U^* = 15.9$, which is $Re = 7.9 \times 10^3$. We thus attribute this second band of frequency as being the footprint left by the shedding of Karman vortices, and the first band as the result of streamwise vortex shedding.

The knowledge that Karman vortices continue to exist and shed from a cruciform structure during SVIV is not new in the literature. However, this is the first time the lift signal from a cruciform structure undergoing SVIV has been subjected to EEMD, revealing the signature of the two dominant vortical structures regulating the flow around

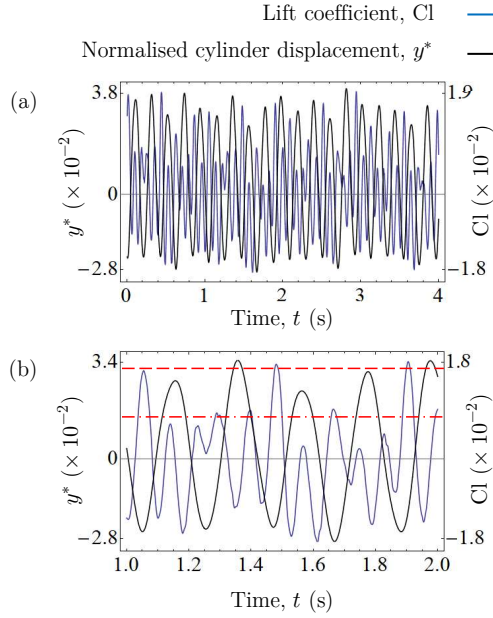


Figure 15: Temporal evolution of y^* and Cl at $U^* 15.9$. Fig. 15b shows an enlarged view of Fig. 15a. We can barely spot semblance of two signals with different amplitudes superimposed in the Cl signal in Fig. 15b.

the cruciform. Although the magnitude of the instantaneous frequency due to Karman vortex is comparable to the streamwise vortex (sometimes even bigger), the reason why the cylinder resists locking into its frequency is perhaps that its frequency too distant from the natural frequency of the system f_n . The shedding frequency of the streamwise vortex is much closer to f_n and is thus preferred by the cylinder.

We consider the transition to SVIV to be complete at $U^* = 18.2$, when the mean phase lag ϕ drops further to ≈ 20 deg. Figure 17a and 17b documents this observation. The phase lag is observed to slip through 360 deg. At certain portions of the characteristic Cl profile where there are slight distortions in the periodicity of the IMF. The slipping through 360 deg. was also observed by Khalak and Williamson (1999) in their work on KVIV, which highlights the quasi-periodic nature of the signal being analysed. There, the slip appeared in Khalak and Williamson (1999) at the initial branch of KVIV. It may be the case that the overall low value of $\phi \approx 20$ deg. at $U^* = 18.2$, coupled with the presence of ϕ slippage is suggesting the possibility of $U^* = 18.2$ being the initial branch for SVIV. We could not foresee this point brought up if the original Cl signal is not decomposed beforehand, implying the utility of EEMD in studying fluid-structure interactions with multiple dominant flow structures.

5.4. The stable SVIV regime ($U^* > 20$)

As U^* is increased to 20.5, we can see a jump in ϕ from a mean value of approximately 20 deg. to about 120 deg., shown in Fig. 18a. The phase slippage discussed previously is also observed in this time series subset, indicating the quasi-periodic nature of the lift coefficient signal at this U^* . Incidentally, this quasi-periodicity seems to be the norm

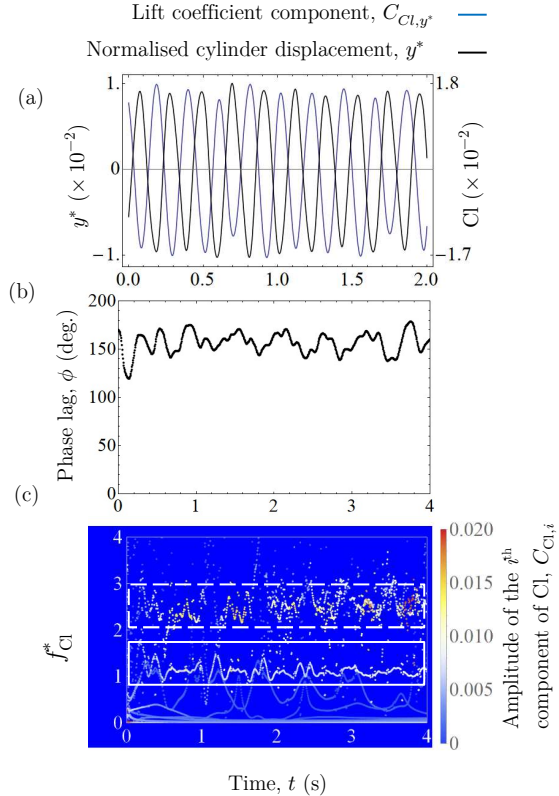


Figure 16: Temporal analysis of the lift component that has the highest correlation to the original (normalised) cylinder displacement signal, C_{Cl,y^*} , and the normalised cylinder displacement signal at $U^* = 15.9$. The component was obtained by decomposing the lift coefficient signal using EEMD. We show C_{Cl,y^*} and y^* signal side by side in Fig. 16a, present the temporal evolution of the phase lag ϕ of C_{Cl,y^*} in Fig. 16b and show the temporal evolution of the instantaneous frequency of the C_{Cl,y^*} in Fig. 16c. The blue line in Fig. 16c represents the lift coefficient component signal, while the black line represents the normalised cylinder displacement.

for the lift signals up to $U^* = 27.3$, as suggested by the phase slippages evident in Figs. 17b, c and d. The slippage only stops once U^* reaches 29.5, suggesting a more periodic behaviour of the lift coefficient compared to its counterparts between $20.5 \leq U^* \leq 27.3$. Although the instantaneous phase between $20.5 \leq U^* \leq 27.3$ implies a quasi-periodic nature, their mean values at each U^* are contained in the narrow region $114 < \phi$ (deg.) < 135 , as is the value for ϕ at $U^* = 29.5$. This observation that the value of ϕ is only slowly varying with respect to U^* , once U^* increases past 20.5, can be interpreted as the dominant flow structures settling into a stable form that becomes more resilient against external excitations. Based on this feature, it seems appropriate to classify $20.5 \leq U^* \leq 29.5$ as the upper branch of SVIV.

Figure 19 summarises our findings thus far, with respect to our analysis of the Cl time series, specifically the ensemble average value of ϕ , denoted as ϕ_{mean} . The region an indicates the initial branch of KVIV, where ϕ_{mean} is close to zero. Region B denotes the upper/lower branch of KVIV, where the system experiences a jump from $\phi_{\text{mean}} \approx 0$ to greater than 110 deg. The value of ϕ_{mean} settles very close to 180 deg. towards the end of this upper/lower branch.

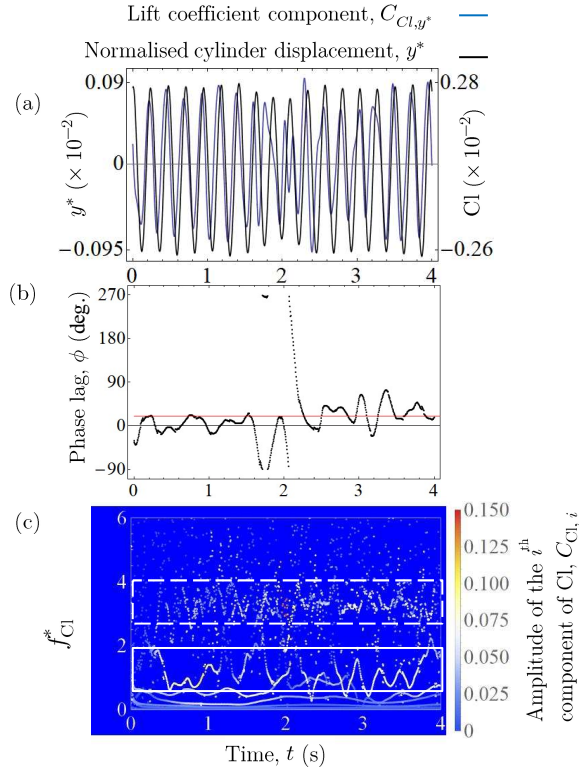


Figure 17: Temporal analysis of the lift coefficient component that has the highest correlation to the original (normalised) cylinder displacement signal, C_{Cl,y^*} , and the normalised cylinder displacement signal at $U^*18.2$. The component was obtained by decomposing the lift coefficient signal using EEMD. We show C_{Cl,y^*} and y^* side by side in Fig. 17a, present the temporal evolution of the phase lag ϕ of C_{Cl,y^*} in Fig. 17b and show the temporal evolution of the instantaneous frequency of the C_{Cl,y^*} in Fig. 17c. The blue line in Fig. 17a represents the lift coefficient component signal, while the black line represents the normalised cylinder displacement.

455 The HHT spectrograms up to this U^* show only one dominant band of f_{Cl}^* which is close to the Strouhal frequency of
 456 Karman vortex shedding.

457 Then, ϕ_{mean} experiences a slight drop of about one-sixth the value of ϕ_{mean} at the preceding upper/lower branch as
 458 we enter region C, marking the start of the transition to the SVIV regime. The emergence of two dominant instantaneous
 459 frequency bands for f_{Cl}^* further supports this demarcation. One of the dominant f_{Cl}^* band has a value close to unity,
 460 and the other has a value close to the shedding frequency of Karman vortex for a fixed, isolated circular cylinder at the
 461 same Reynolds number. The system then undergoes a more sudden drop to $\phi_{\text{mean}} \approx 20$ deg. at $U^* = 18.2$. Inspecting
 462 the temporal evolution of ϕ revealed the quasi-periodic nature of Cl at this U^* , which is analogous to the KVIV initial
 463 branch studied by Khalak and Williamson (1999), prompting us to assign the region up to $U^* = 20.5$ as the initial
 464 branch of SVIV (region D).

465 Finally, in region E, we observe another jump in ϕ_{mean} from $\phi_{\text{mean}} \approx 20$ deg. to approximately 120 deg. as
 466 $U^* > 20.5$. The Cl signal gradually loses its quasi-periodicity with increasing U^* , and the ϕ_{mean} in this region falls

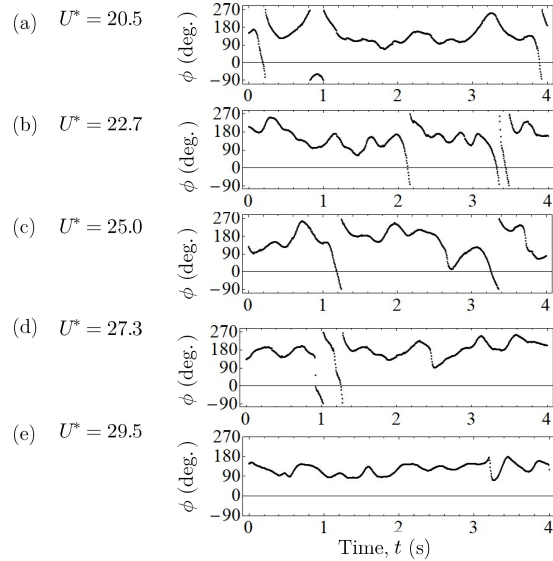


Figure 18: The instantaneous phase lag ϕ of the dominant component of the normalised cylinder displacement signal (y^*) against C_{Cl,y^*} in the range $20 < U^* < 30$. See Fig. 17 for the definition of C_{Cl,y^*} .

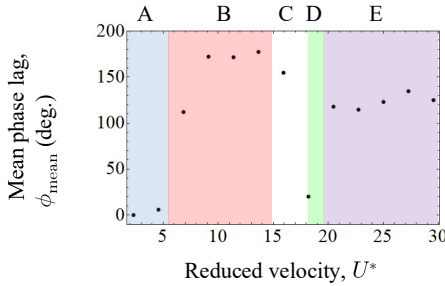


Figure 19: Vibration regimes identified during analysis of ϕ . To capture the evolution of ϕ with respect to U^* , a representative value for ϕ at each U^* must be selected. We chose to use the mean ϕ as the representative value.

467 within the arguably narrow range of $114 < \phi$ (deg.) < 135 , pointing to stabilisation of dominant flow structures. We
 468 hence designate region E as the upper branch of SVIV.

469 6. Estimation of harnessable power

470 6.1. Mathematical model for power estimation

471 The mathematical model for harnessable power estimation in this study follows that which had been derived in
 472 Raghavan et al. (2007). In these works, the authors mentioned that work done by the oscillating cylinder W_{cyl} during

473 one cycle of oscillation $T_{\text{osc.}}$ is as follows.

$$W_{\text{cyl.}} = \int_0^{T_{\text{osc.}}} (F_L \cdot \dot{y}) dt \quad (24)$$

474 where both the lift F_L and cylinder velocity \dot{y} are both functions of time. Through several manipulations and
 475 simplifying assumptions (Sun et al., 2016), the power captured by the system can be written, using our parameters, as
 476 the fluid power

$$P_{\text{Fluid,RMS}} = \frac{1}{2} \rho \pi C_{\text{Cl,RMS}} U^2 f_{\text{osc.}} y_{\text{RMS}}^* D L \sin(\phi), \quad (25)$$

477 or the mechanical power

$$P_{\text{Mech.,RMS}} = 8\pi^3 m_{\text{eff.}} \zeta_{\text{tot.}} (y_{\text{RMS}}^* f_{\text{osc.}})^2 f_n. \quad (26)$$

478 Here, $P_{\text{Fluid,RMS}}$, $P_{\text{Mech.,RMS}}$, L , $C_{\text{Cl,RMS}}$, $\zeta_{\text{tot.}}$ and $m_{\text{eff.}}$ are the root mean square of fluid power, root mean square
 479 of mechanical power, length of the circular cylinder, characteristic root mean square of lift amplitude, total damping
 480 coefficient, and the system effective mass respectively. We choose to use root mean square (parameters with subscript
 481 RMS) quantities in Eq. 24 instead of the maximum values like the original authors because that may lead to a misun-
 482 derstanding that the maximum value is sustained throughout the observation window. This obviously is not always the
 483 case in our study, especially once the flow transits to SVIV. Time series analysis of $y^*(t)$ and $\text{Cl}(t)$ in §4.1 revealed
 484 that there is a degree of intermittency in both signals that cannot be overlooked at specific ranges of U^* , thus making
 485 it better to use the root mean square values instead. Estimation of the root mean square of harnessable power in our
 486 opinion makes more sense because it returns a value that is continually approached by the system *over time*, while the
 487 maximum, could be a one-off value.

488 Before presenting the results of our harnessable power estimation following Eqs. 25 and 26, let us clarify our
 489 method of estimating the root mean square of lift amplitude $C_{\text{Cl,RMS}}$. Let $F_L(t)$ be the lift acting on the cylinder and
 490 $y(t)$ the cylinder displacement time series resulting from that alternating lift. Decomposing $F_L(t)$ via EEMD yields a
 491 finite number N of IMFs which we can summarily write as $F_L(t) = \sum_i^N C_i(t)$. The IMF chosen as the component of
 492 lift driving $y(t)$ is the $C_i(t)$ with the highest correlation with $y(t)$, i.e. the component due to streamwise vortex. We
 493 then compute the root mean square value of that component of lift, giving us $C_{\text{Cl,RMS}}$.

- $P_{\text{Mech.,RMS}}$, current study (experiment)
- $P_{\text{Fluid,RMS}}$, current study (numerical)
- $P_{\text{Mech.,RMS}}$, current study (numerical)
- ▶ $P_{\text{Measured,RMS}}$, Koide et al. (2013) (experiment)
- △ $P_{\text{Mech.,RMS}}$, Nguyen et al. (2012) (experiment)

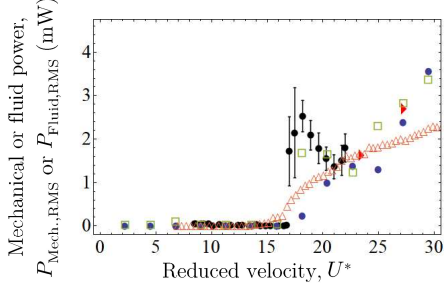


Figure 20: Estimated root mean square of mechanical power $P_{\text{Mech.,RMS}}$, fluid power $P_{\text{Fluid,RMS}}$, or both, of our experimental and numerical results, compared with results of similar studies in the literature. The fluid power $P_{\text{Fluid,RMS}}$ is calculated only from the results of our numerical study as the others did not measure lift. The computation of the instantaneous phase lag ϕ requires both lift and cylinder displacement signals.

494 Figure 21 shows the comparison between power estimated from our experiment and numerical results, with the
 495 experimental results of Nguyen et al. (2012) and the direct power measurement of Koide et al. (2013). Only the value
 496 for $P_{\text{Mech.,RMS}}$ is computed from our experimental results due to the absence of lift data. Our numerical results have
 497 both lift and cylinder displacement data, and hence, we calculated both $P_{\text{Fluid,RMS}}$ and $P_{\text{Mech.,RMS}}$. We estimated the
 498 power from the experimental results of Nguyen et al. (2012) by interpolating missing data points in both their amplitude
 499 and frequency responses to compute the value of $P_{\text{Mech.,RMS}}$ at a given value of U^* . The direct power measurement
 500 by Koide et al. (2013) was done by connecting the elastic support of the cylinder to a coil. The coil moves with the
 501 cylinder, thus creating a relative pistoning motion against a fixed magnet and produces an alternating current.

502 We note that the evolution trend of estimated power with respect to U^* is similar between $P_{\text{Mech.,RMS}}$ from our
 503 experiment and simulation, especially in the U^* region immediately after the onset of SVIV. This makes sense since
 504 $P_{\text{Mech.,RMS}}$ is basically a single variable function, the variable being y_{RMS}^* , with the others fixed as we vary U^* . The
 505 trend observed in $P_{\text{Mech.,RMS}}$ is thus a scaled version of the trend found in y_{RMS}^* . Nevertheless, besides this region of
 506 $18 < U^* < 23$ the trend between all data series compared in Fig. 21 are relatively similar. This trend is especially
 507 the case after $U^* > 23$, where we observe a fairly good agreement between $P_{\text{Mech.,RMS}}$ and $P_{\text{Fluid,RMS}}$ computed from
 508 our experimental and numerical results with the direct power measurements of Koide et al. (2013) and the estimated
 509 $P_{\text{Mech.,RMS}}$ from the data of Nguyen et al. (2012). The estimated power in the KVIV regime $U^* < 17$ produces power
 510 only in the order of μW , which is relatively insignificant in contrast to the magnitude of power produced in the SVIV
 511 regime (mW).

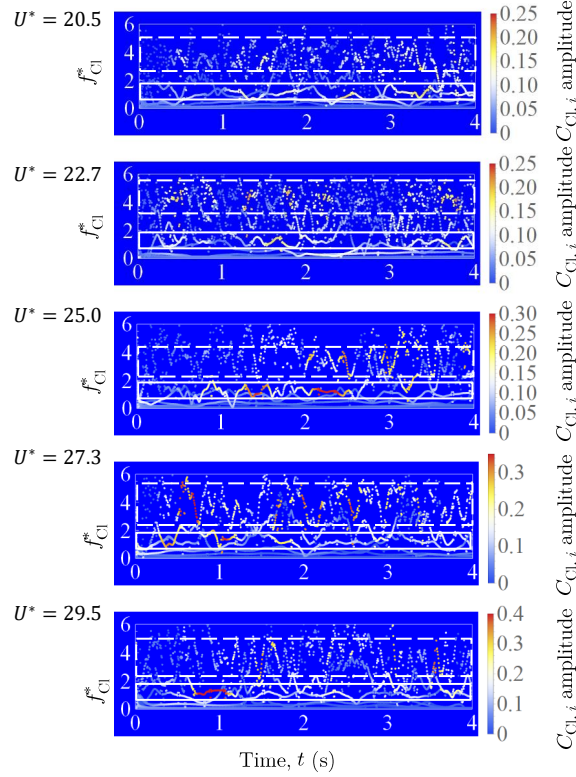


Figure 21: The instantaneous frequency of the lift signal between $20 < U^* < 30$. The white, solid box encloses the region where the mean frequency is close to the system natural frequency f_n , while the dashed, white box encloses the region where the mean frequency is close to the shedding frequency of Karman vortex at the Reynolds number at which the simulation is performed. Through visual inspection, we can see how the degree of dispersion in the instantaneous frequency of the “Karman component” of lift is about twice that of the “streamwise component” of lift.

512 6.2. Possibility for increasing fluid power, $P_{\text{Fluid,RMS}}$

513 We have seen in Fig. 20 the similarity in the evolution trend of $P_{\text{Mech.,RMS}}$ and $P_{\text{Fluid,RMS}}$ against U^* of our
 514 numerical results with those from Nguyen et al. (2012) and Koide et al. (2013). However, recall that to represent the
 515 amplitude of lift, we used the root mean square amplitude of the component of lift that has the highest correlation with
 516 the original cylinder displacement signal $y(t)$. We did not use the root mean square amplitude of the original lift signal,
 517 and yet we obtained $P_{\text{Fluid,RMS}}$ estimates that are in reasonable agreement not only with its $P_{\text{Mech.,RMS}}$ counterparts but
 518 with the actual measured power of Koide et al. (2013).

519 On the one hand, this is an indication that the lift component selected for use in computation is an arguably faithful
 520 representation of the force driving the motion of the cylinder. The fact that it is a reasonably good representation also
 521 suggests that the motion of the cylinder, once it enters the SVIV regime, is driven only by a subset of the total lift force.
 522 Another significant subset of the lift force is the component whose mean frequency is close to the Karman frequency
 523 of vortex shedding, as explained in §5.3. This Karman component of lift has a similar order of magnitude to the
 524 streamwise vortex component (or just streamwise component for short) of lift, as evidenced in Fig. 21, and is therefore

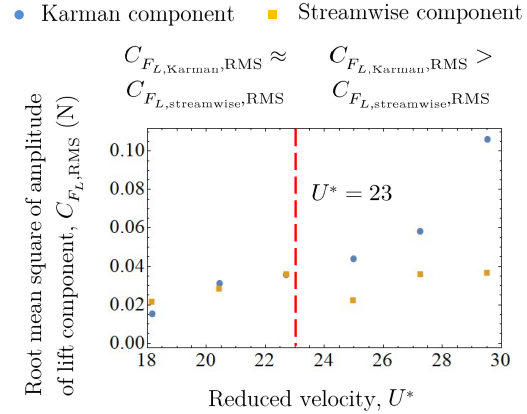


Figure 22: Evolution of the root mean square amplitude of two dominant lift components, Karman and streamwise vortices with respect to U^* . The region $U^* < 23$ exhibits similar magnitude for both the Karman and streamwise components of lift. On the other hand, the magnitude of amplitude for the Karman component while the region $U^* > 23$ is almost always twice that of the streamwise component.

not negligible. The Karman components are marked with a dashed, white box, and the streamwise components are marked with a solid, white box, following the convention in Figs. 12, 13, 14, 16 and 17. However, the Karman component fails to affect the cylinder vibration like the streamwise component most probably due to the large difference between the mean frequency of the Karman component and the natural frequency of the system, f_n . The streamwise component has a mean frequency close to f_n and is hence able to synchronise with the vibration of the cylinder, producing a sizeable amplitude response.

Figure 22 shows the root-mean-square amplitude of the Karman and streamwise components of lift in the SVIV regime $U^* > 18$. Between $18 < U^* < 23$, the magnitude of the Karman and streamwise components are nearly equal. However, once we exceed $U^* = 23$, Fig. 22 shows that the contribution to the root-mean-square amplitude of total lift by the Karman component is on average twice the contribution of the streamwise component. Let us assume a hypothetical situation where we can transfer the contribution by the Karman component to the streamwise component of lift. Then, the value for $C_{Cl,RMS}$ in Eq. 25 will increase close to a factor of 2 when $18 < U^* < 23$, and close to a factor of 3 when $23 < U^* < 30$. This increase in $C_{Cl,RMS}$ will lead to a larger $P_{Fluid,RMS}$, if the value of the other parameters in Eq. 25 are similar. The point of this exercise is to demonstrate a procedure to estimate the room for improvement for future developments of the cruciform system concerning $P_{Fluid,RMS}$.

7. Conclusions

In this study, we numerically investigated the temporal evolution of the lift coefficient and cylinder displacement signals of an elastically supported cruciform system in the range $1.1 \times 10^3 < Re < 14.6 \times 10^3$, or $2.3 < U^* < 29.5$. Our circular cylinder diameter is 10 mm and the natural frequency of the system is 4.4 Hz. Validation of key numerical

544 results was made experimentally in a custom-built open flow channel, using a cruciform system whose parameters
 545 were tuned as close as possible to the quantities used in the numerical study.

546 We observed the amplitude response to reach large magnitudes when the dominant frequency of lift is close to the
 547 natural frequency of the system, i.e. f_n . This observation explains the maxima in the amplitude response at $U^* = urth$,
 548 which takes place at the upper branch of the KVIV regime, i.e. $2.3 \leq U^* \leq 13.6$. The onset of streamwise vortex shedding
 549 imposes an additional degree of complexity on the lift coefficient signal, causing it to deviate from the sinusoidal-like
 550 signature of lift observable in the KVIV regime. This complexity is, however, not observed in the cylinder displacement
 551 signal, which remains relatively similar to a sinusoidal function. Decomposing the lift coefficient signal in the SVIV
 552 regime ($15.9 \leq U^* \leq 29.5$) using EEMD allows us to see that the complexity of the lift coefficient signal as probably
 553 being caused by the superimposition of two dominant components of lift. One due to the shedding of Karman and the
 554 other due to the shedding of streamwise vortices. This component of lift has a mean frequency close to f_n . Through
 555 visual inspection, it is relatively similar to a sinusoidal function. This sinusoidal profile results in a similar pattern in
 556 the cylinder displacement signal in the SVIV regime.

557 Application of the Hilbert-Huang transform on the most dominant component of cylinder displacement – and the
 558 component of lift most correlated to it – allows for the computation of the instantaneous phase lag between lift and
 559 cylinder displacement. The temporal mean of the instantaneous phase lag revealed five “branches” of vibration, among
 560 which is the initial branch of SVIV at $U^* = 18.2$, which has never been identified before in the literature.

561 Estimation of power from our results show that the root-mean-square mechanical and fluid power computed from
 562 our numerical work to be in fairly good agreement with the root-mean-square mechanical power computed from our
 563 experiments. There are, however, discrepancies with the trend found in other literature, especially within $15.9 \leq U^* \leq$
 564 20.5, which is right after the onset of SVIV. These discrepancies are probably due to deviations from the literature in
 565 terms of the fluid environment we subject the cruciform system to during data collection (open flow channel v.s. water
 566 tunnel, medium flow turbulence v.s. low flow turbulence). Finally, we estimated the upper limit for improvement of
 567 the root-mean-square fluid/mechanical power and found that the root-mean-square powers can potentially be increased
 568 close to a factor of 2 within $18 < U^* < 23$ and close to a factor of 3 when $23 < U^* < 30$. We base the estimation
 569 on the ability to minimise the contribution from Karman vortices, while maximising the contribution from streamwise
 570 vortices towards the total root-mean-square lift amplitude.

571 References

- 572 Ali, M.S.M., Doolan, C.J., Wheatley, V., 2012. Low Reynolds number flow over a square cylinder with a detached flat plate. International
 573 Journal of Heat and Fluid Flow 36, 133–141. URL: <http://dx.doi.org/10.1016/j.ijheatfluidflow.2012.03.011>, doi:10.1016/j.
 574 ijheatfluidflow.2012.03.011.

Lift Evolution in a Pure Cruciform Energy Harvester

- 575 Bernitsas, M., Raghavan, K., 2008. Reduction/suppression of VIV of circular cylinders through roughness distribution at $8 \times 10^3 < Re < 1.5 \times 10^5$,
576 in: Proceedings of the International Conference on Offshore Mechanics and Arctic Engineering - OMAE.
- 577 Bernitsas, M.M., Ben-Simon, Y., Raghavan, K., Garcia, E.M.H., 2009. The VIVACE Converter: Model Tests at High Damping and
578 Reynolds Number Around 10^5 . Journal of Offshore Mechanics and Arctic Engineering 131. URL: <http://offshoremecanics.asmedigitalcollection.asme.org/article.aspx?articleid=1472649>, doi:10.1115/1.2979796.
- 580 Bernitsas, M.M., Raghavan, K., Ben-Simon, Y., Garcia, E.M.H., 2008. VIVACE (Vortex Induced Vibration Aquatic Clean Energy): A New
581 Concept in Generation of Clean and Renewable Energy From Fluid Flow. Journal of Offshore Mechanics and Arctic Engineering 130,
582 041101. URL: <http://www.scopus.com/record/display.url?eid=2-s2.0-56749179917&origin=resultslist&sort=plf-f&src=s&st1=A+new+concept+in+generation+of+clean+and+renewable+energy+from+fluid+flow&sid=620865A71FAF26768C42655E1E8BC194.aXczxbyuHHiXgaIW6Ho7g:230&sot=b&sdt=b&h>, doi:10.1115/1.2957913.
- 585 Blevins, R.D., 1990. Flow-induced vibration .
- 586 Deng, J., Ren, A.L., Shao, X.M., 2007. The flow between a stationary cylinder and a downstream elastic cylinder in cruciform arrangement.
587 Journal of Fluids and Structures 23, 715–731. URL: <https://www.sciencedirect.com/science/article/pii/S0889974606001472>,
588 doi:10.1016/J.JFLUIDSTRUCTS.2006.11.005.
- 589 Ding, L., Bernitsas, M.M., Kim, E.S., 2013. 2-D URANS vs. experiments of flow induced motions of two circular cylinders in tandem with
590 passive turbulence control for 30,000. Ocean Engineering 72, 429–440. URL: <http://www.sciencedirect.com/science/article/pii/S0029801813002448?via%23Dihub>, doi:10.1016/J.OCEANENG.2013.06.005.
- 592 Ding, L., Zhang, L., Kim, E.S., Bernitsas, M.M., 2015a. URANS vs. experiments of flow induced motions of multiple circular cylinders with
593 passive turbulence control. Journal of Fluids and Structures 54, 612–628. doi:10.1016/j.jfluidstructs.2015.01.003.
- 594 Ding, L., Zhang, L., Wu, C., Mao, X., Jiang, D., 2015b. Flow induced motion and energy harvesting of bluff bodies with different cross sections.
595 Energy Conversion and Management doi:10.1016/j.enconman.2014.12.039.
- 596 Ding, W., Sun, H., Xu, W., Bernitsas, M.M., 2019. Numerical investigation on interactive FIO of two-tandem cylinders for hydrokinetic energy
597 harnessing. Ocean Engineering 187, 106215. URL: <https://www.sciencedirect.com/science/article/pii/S0029801819304019>,
598 doi:10.1016/J.OCEANENG.2019.106215.
- 599 Gumarlar, A.B., Purnomo, M.H., Yuniarso, E.M., Sugiarto, I., 2019. Spectral Analysis of Familiar Human Voice Based On Hilbert-Huang Transform,
600 in: 2018 International Conference on Computer Engineering, Network and Intelligent Multimedia, CENIM 2018 - Proceeding. doi:10.1109/CENIM.2018.8710943.
- 602 Hemsuwan, W., Sakamoto, K., Takahashi, T., 2018. Numerical investigation of lift-force generation on a moving circular cylinder in a uniform flow
603 driven by longitudinal vortex. Journal of Fluids and Structures 83, 448–470. URL: <https://www.sciencedirect.com/science/article/pii/S0889974617308885>, doi:10.1016/J.JFLUIDSTRUCTS.2018.09.010.
- 605 Huang, N.E., 2014. Hilbert-Huang transform and its applications. volume 16. World Scientific.
- 606 Huang, N.E., Attoh-Okine, N.O., 2005. The Hilbert-Huang transform in engineering. CRC Press.
- 607 Huang, N.E., Shen, Z., Long, S.R., Wu, M.C., Srinivasa, H.H., Zheng, Q., Yen, N.C., Tung, C.C., Liu, H.H., 1998. The empirical mode decomposition
608 and the Hilbert spectrum for nonlinear and non-stationary time series analysis. Proceedings of the Royal Society A: Mathematical, Physical and
609 Engineering Sciences doi:10.1098/rspa.1998.0193.
- 610 Kawabata, Y., Takahashi, T., Hagiwara, T., Shirakashi, M., 2013. Interference Effect of Downstream Strip-Plate on the Crossflow Vibration of a
611 Square Cylinder. Journal of Fluid Science and Technology 8, 647–658. doi:10.1299/jfst.8.348.
- 612 Khalak, A., Williamson, C., 1999. Motions, Forces And Mode Transitions In Vortex-Induced Vibrations At Low Mass-Damping. Journal of Flu-

Lift Evolution in a Pure Cruciform Energy Harvester

- 613 ids and Structures 13, 813–851. URL: <http://www.sciencedirect.com/science/article/pii/S0889974699902360>, doi:10.1006/jfls.1999.0236.
- 614 Koide, M., Kato, N., Yamada, S., Kawabata, Y., Takahashi, T., Shirakashi, M., 2007. Influence Of A Cruciform Arrangement Downstream Strip-Plate On Crossflow Vibration. Journal of Computational and Applied Mechanics 8, 135–148.
- 615 Koide, M., Ootani, K., Yamada, S., Takahashi, T., Shirakashi, M., 2006. Vortex Excitation Caused by Longitudinal Vortices Shedding from
- 616 Cruciform Cylinder System in Water Flow. JSME International Journal 49, 1043–1048.
- 617 Koide, M., Sekizaki, T., Yamada, S., Takahashi, T., Shirakashi, M., 2009. A Novel Technique for Hydroelectricity Utilizing Vortex Induced
- 618 Vibration, in: Proceedings of the ASME Pressure Vessels and Piping Division Conference, PVP2009-77487.
- 619 Koide, M., Sekizaki, T., Yamada, S., Takahashi, T., Shirakashi, M., 2013. Prospect of Micro Power Generation Utilizing VIV in Small
- 620 Stream Based on Verification Experiments of Power Generation in Water Tunnel. Journal of Fluid Science and Technology 8, 294–
- 621 308. URL: <https://www.jstage.jst.go.jp/article/jfst/8/3/8{ }294/{}article> http://jlc.jst.go.jp/DN/JST.JSTAGE/jfst/8.294?lang=en&from=CrossRef&type=abstract, doi:10.1299/jfst.8.294.
- 622 Koide, M., Takahashi, T., Shirakashi, M., Salim, S.A.Z.B.S., 2017. Three-dimensional structure of longitudinal vortices shedding from cruciform
- 623 two-cylinder systems with different geometries. Journal of Visualization , 1–11.
- 624 Langley Research Centre, 2018. Turbulence Modeling Resource. URL: <https://turbmodels.larc.nasa.gov/>.
- 625 Li, X., Lyu, Z., Kou, J., Zhang, W., 2019. Mode competition in galloping of a square cylinder at low Reynolds number. Journal of Fluid Mechanics
- 626 867, 516–555. URL: <https://www.cambridge.org/core/product/identifier/S0022112019001605/type/journal{ }article>, doi:10.1017/jfm.2019.160.
- 627 Maruai, N.M., Ali, M.S.M., Ismail, M.H., Zaki, S.A., 2018. Flow-induced vibration of a square cylinder and downstream
- 628 flat plate associated with micro-scale energy harvester. Journal of Wind Engineering and Industrial Aerodynamics 175, 264–
- 629 282. URL: <https://www.scopus.com/inward/record.uri?eid=2-s2.0-85042219159&doi=10.1016%2Fj.jweia.2018.01.010&partnerID=40&md5=2f3f62b94bb69ced3368b32e682aefc7>, doi:10.1016/j.jweia.2018.01.010.
- 630 Maruai, N.M., Mat Ali, M.S., Ismail, M.H., Shaikh Salim, S.A.Z., 2017. Downstream flat plate as the flow-induced vibration enhancer for energy harvesting. Journal of Vibration and Control , 1077546317707877URL: <http://journals.sagepub.com/doi/10.1177/1077546317707877>, doi:10.1177/1077546317707877.
- 631 Mat Ali, M.S., Doolan, C.J., Wheatley, V., 2011. Low Reynolds number flow over a square cylinder with a splitter plate. Physics of Fluids 23,
- 632 doi:10.1063/1.3563619.
- 633 Nguyen, T., Koide, M., Yamada, S., Takahashi, T., Shirakashi, M., 2012. Influence of mass and damping ratios on VIVs of a cylinder with a
- 634 downstream counterpart in cruciform arrangement. Journal of Fluids and Structures 28, 40–55. doi:10.1016/j.jfluidstructs.2011.10.006.
- 635 Raghavan, K., 2007. Energy Extraction from a Steady Flow Using Vortex Induced Vibration. Doctoral dissertation. The University of Michigan.
- 636 URL: <http://deepblue.lib.umich.edu/handle/2027.42/55687>.
- 637 Raghavan, U., Albert, R., Kumara, S., 2007. Near linear time algorithm to detect community structures in large-scale networks. Phys. Rev E. 76,
- 638 036106.
- 639 Richardson, L.F., Gaunt, J.A., 1927. The deferred approach to the limit. Philosophical Transactions of the Royal Society A doi:<https://doi.org/10.1098/rsta.1927.0008>.
- 640 Shirakashi, M., Mizuguchi, K., Bae, H.M., 1989. Flow-induced excitation of an elastically-supported cylinder caused by another located downstream
- 641 in cruciform arrangement. Journal of Fluids and Structures 3, 595–607. doi:10.1016/S0889-9746(89)90150-3.
- 642
- 643
- 644
- 645
- 646
- 647
- 648
- 649
- 650

Lift Evolution in a Pure Cruciform Energy Harvester

- 651 Stern, F., Wilson, R.V., Coleman, H.W., Paterson, E.G., 2001. Comprehensive approach to verification and validation of CFD simulations^{if};part 1:
652 methodology and procedures. *Journal of fluids engineering* 123, 793–802.
- 653 Sun, H., Kim, E.S., Nowakowski, G., Mauer, E., Bernitsas, M.M., 2016. Effect of mass-ratio, damping, and stiffness on optimal hydrokinetic energy
654 conversion of a single, rough cylinder in flow induced motions. *Renewable Energy* 99, 936–959. URL: <http://www.sciencedirect.com/science/article/pii/S0960148116306206>, doi:10.1016/j.renene.2016.07.024.
- 655 Wang, S., Wen, F., Shi, X., Zhou, X., 2019. Stability analysis of asymmetric wakes. *Physics of Fluids* doi:10.1063/1.5098111.
- 656 Wu, W., 2011. Two-Dimensional RANS Simulation of Flow Induced Motion of Circular Cylinder with Passive Turbulence Control. Doctoral
657 dissertation. The University of Michigan.
- 658 Wu, Z., Huang, N.E., 2008. Ensemble Empirical Mode Decomposition: A Noise-Assisted Data Analysis Method. *Advances in Adaptive Data
659 Analysis* doi:10.1142/s1793536909000047.
- 660 Zhang, B., Mao, Z., Song, B., Ding, W., Tian, W., 2018. Numerical investigation on effect of damping-ratio and mass-ratio on energy
661 harnessing of a square cylinder in FIM. *Energy* 144, 218–231. URL: [https://www.scopus.com/inward/record.uri?eid=2-s2.0-85037995662&doi=10.1016%2Fj.energy.2017.11.153](https://www.scopus.com/inward/record.uri?eid=2-s2.0-85037995662&doi=10.1016%2Fj.energy.2017.11.153&partnerID=40&md5=01db7c6b6d4d44e88de7045843c7d423), doi:10.1016/j.energy.2017.11.153.
- 661 Zhao, M., Lu, L., 2018. Numerical simulation of flow past two circular cylinders in cruciform arrangement. *Journal of Fluid Mechanics* 848, 1013–
662 1039. URL: https://www.cambridge.org/core/product/identifier/S0022112018003804/type/journal_article, doi:10.
663 1017/jfm.2018.380.
- 664 Zhou, L., Meng, Y., Abbaspour, K.C., 2019. A new framework for multi-site stochastic rainfall generator based on empirical orthogonal function
665 analysis and Hilbert-Huang transform. *Journal of Hydrology* doi:10.1016/j.jhydrol.2019.05.047.